isvr Institute of Sound and Vibration Research

A RANS CFD Coupled Model for Predicting Coaxial Jet Noise

R. H. Self

ISVR Technical Report No 304

January 2005

University of Southampton

SCIENTIFIC PUBLICATIONS BY THE ISVR

Technical Reports are published to promote timely dissemination of research results by ISVR personnel. This medium permits more detailed presentation than is usually acceptable for scientific journals. Responsibility for both the content and any opinions expressed rests entirely with the author(s).

Technical Memoranda are produced to enable the early or preliminary release of information by ISVR personnel where such release is deemed to the appropriate. Information contained in these memoranda may be incomplete, or form part of a continuing programme; this should be borne in mind when using or quoting from these documents.

Contract Reports are produced to record the results of scientific work carried out for sponsors, under contract. The ISVR treats these reports as confidential to sponsors and does not make them available for general circulation. Individual sponsors may, however, authorize subsequent release of the material.

UNIVERSITY OF SOUTHAMPTON

INSTITUTE OF SOUND AND VIBRATION RESEARCH

FLUID DYNAMICS AND ACOUSTICS GROUP

A RANS CFD Coupled Model for Predicting Coaxial Jet Noise

by

R H Self

ISVR Technical Report No. 304

January 2005

Authorized for issue by
Professor R J Astley, Group Chairman

Contents

1 Introduction

This paper describes an acoustic prediction scheme for the far field noise spectra of coaxial jets that uses a Reynolds Averaged Navier-Stokes CFD (with k-ϵ turbulence model) prediction of the coaxial jet turbulent flow as input to an advanced noise model. Previous work by the author and others [25, 21] has demonstrated the applicability of such a method to the prediction of single-stream isothermal jet noise and coaxial jet noise at a far-field observation angle of 90° to the jet axis. The present work improves the theoretical basis of the model and increases the range of applicability by computing the far-field acoustic spectra of a number of isothermal coaxial jet configurations over a range of observation angles. The motivation for developing this methodology comes from the continuing importance of jet noise as a major component of the noise emission from civil turbofan aircraft, and the requirement to find accurate and reliable methods for predicting it.

The most general methodology for the prediction of far-field jet noise of jets involves a computation of the near-field unsteady flow-field using either a DNS or LES technique in conjunction with an acoustic analogy. Whilst such an approach has many advantages, the inability to perform the necessary numerically intensive calculations quickly is a severe limitation for using it as an engineering design aid. Equally, many current LES methods would be unable to handle the complex geometric features, such as serrations, of modern noise reducing engine nozzles. An alternative approach, discussed in this paper, is to couple the output of a fast running CFD code, such as a Reynolds Averaged Navier-Stokes (RANS) (using an appropriate turbulence model) to an acoustic source model in order to predict the far-field noise of the jet. (See, for example, references [27] and [26].)

The acoustic model chosen is based on an Acoustic Analogy formalism. The first statement of such an analogy was given by Lighthill [13, 14] who rearranged the full equations of motion in the form of a linear wave equation, with equivalent acoustic sources that depend on the mean and turbulent flow fields. The basic philosophy of Lighthill's Acoustic Analogy assumes that once the flow variables have been used to calculate the equivalent acoustic sources, the underlying flow has little or no influence on the subsequent acoustic problem. However, Lighthill quickly recognised the need to account for effects arising from the fact that the acoustic sources are being convected by the mean flow of the jet, and this led him to introduce a convective amplification factor comprising of the reciprocal of six powers of Doppler factor. Subsequently, Ffowcs Williams [4] argued that because of the limited spatial extent of the jet, the convective amplification factor should comprise the reciprocal of five powers of Doppler factor.

While source convection effects (and source non-compactness effects which are discussed below) can be adequately incorporated into Lighthill's analogy, the subsequent theory neglects refraction of sound away from the jet axis [23] due to flow-acoustic interaction. As was demonstrated by Lush [16] this is of significant importance for high velocity jets and for observer angles away from 90 degrees to the jet axis. In order to incorporate flow-acoustic interaction effects Lilley [15] reformulated the acoustic analogy in a way which more clearly separated the noise generation from the subsequent interaction between acoustic waves and the mean flow field of the jet. The third order convected wave equation that results from Lilley's Acoustic

Analogy was considered by Tester and Morfey [28] who obtained a solution for a specific class of shear layer. In analogy to the convective amplification factor, Tester and Morfey introduced the notion of a flow factor that multiplies the no-flow solution to account for flow-acoustic interaction effects.

The development of the acoustic model described below broadly follows this approach. The basic source model is considered using the Lighthill equation and incorporates directivity arising from source non-compactness effects. Subsequently, source convection and flow-acoustic interaction effects are accounted for by incorporating appropriate directivity factors. However, apart from developing an acoustic model, there is also the important question of coupling it to the RANS output, and this is a far from trivial exercise. While RANS CFD with k-ϵ turbulence model predicts the steady mean flow-field and the time averaged behaviour of the turbulence flow field, acoustic analogies require a knowledge of the unsteady properties of the turbulence. In particular, the acoustic sources depend on the cross-correlations of the Reynold's stresses. It is therefore necessary to develop an appropriate model of of these correlations and subsequently relate this model to the time-averaged turbulence properties predicted by the RANS k-ϵ CFD code.

A number of authors have suggested methods for accomplishing this task, some of which have been discussed critically by Morris and Farassat [18]. An early example is represented by the work of Mani, Gliebe and Balsa [1, 22], subsequently developed by Khavaran [10, 11] to use a RANS solution based on a k-ϵ turbulence model (the MGBK method). More recent examples are the work of Tam and Auriault [27] and Woodruff *et. al.* [29]. In the various theories of these authors it is assumed that the temporal behaviour of the cross-correlation function can be adequately described using a time constant that depends linearly on the timescale obtained from the turbulence model ($\tau_{CFD} = \epsilon/k$). Recently, it has been demonstrated by the author [24] that the use of a frequency dependent timescale in the two-point space-time correlation function leads to far better agreement with measured data than an equivalent source term using a constant timescale. The analysis was based on a model jet single stream jet with mean and turbulent flow fields described analytically and approximated the jet as an equivalent line source distribution, and was confined to noise emitted at 90° to the jet axis. In this present paper, a fully 3-dimensional theory is presented with the acoustic source density being dependent on the local properties of the turbulence. Source convection and flow-acoustic interaction effects are included and the theory is applied to a number of (isothermal) coaxial jet configurations.

The layout of the paper is as follows. In the next section we consider Lighthill's Acoustic Analogy as applied to jet noise and; with the object of allowing a later comparison with the solution to Lilley's equation, we start by giving the formal solution in terms of Green's functions. This is followed by the derivation of a far-field analytic solution suitable for incorporation into the computer based prediction method. At this stage there are several unknown parameters and the following section considers how this are best modelled, and how they relate to the CFD output.

Lilley's equation is considered in section 4, and by comparing the formal solutions with those of Lighthill's equation, it is demonstrated that the flow-acoustic effects inherent in Lilley's

equation, but absent from Lighthill's[1], can be accounted for by means of a Flow Factor applied to the Lighthill solution. Analytic forms for the flow factor are exhibited in the limits of high and low frequency of radiated sound. By proceeding in this way (as opposed to using the Lilley equation from the outset) we obtain a prediction theory that combines the relative simplicity and physical transparency of Lighthill's approach with a compact and readily implemented form for the directivity calculation that is crucial for engineering applications. This combined prediction scheme is summarised in section 5. Lastly, section 6 briefly considers the CFD that is used as input and completes the theoretical sections.

The accuracy of the model in predicting the noise from coaxial jets is analysed by a series of comparisons with experimental data and and the results of existing prediction schemes.

The far-field acoustic intensity spectra at a series of differing angles to the jet axis has been made for coaxial jet configurations where experimental data is available. The configurations studied are isothermal coplanar jets with area ratios 2 and 4, and velocity ratios 0.6 and 0.8, and angles range from 30° to 120° to the axis.[2] Overall the accuracy of the prediction is very good, being typically a few dB at worst (but occasionally a more marked departure from the measured data is observed) and the predicted spectra are seen to reproduce the variations in spectral shape as the observation angle is changed extremely well.

A number of comparisons have also been made between the calculated axial source density and measured axial source images and these are followed by a comparison between the axial source density predicted by the present theory with that inferred from an existing semi-empirical prediction scheme. These comparisons prove to somewhat problematic and raise a number of interesting questions that are discussed together with other relevant issues in the final section of the paper.

[1]Since both Lighthill's and Lilley's Acoustic Analogies are arrived at by a rearrangement of the equations of motion they are equivalent. However, it is normal practice to make certain simplifying assumptions about the source terms that has the effect of removing the flow-acoustic effects from Lighthill's equation.

[2]The area ratio is defined as the ratio of the secondary nozzle outlet area to the primary nozzle outlet area. The velocity ratio is the ratio of secondary to primary outlet velocities, and angles are measured with the downstream direction being zero degrees.

2 Lighthill's Analogy and the Acoustic Source Model

As stated in the introduction, the approach taken in this paper is to use Lighthill's version of the Acoustic Analogy to model the acoustic sources in the jet, but including inherent source directivity effects, and account for the remaining directivity effects by means of a flow factor that is arrived at by consideration of Lilley's version of the Acoustic Analogy. While it would be possible to formulate the solution completely in terms of Lilley's equation, the mathematically simpler Lighthill equation affords greater clarity to the arguments.

Lighthill's equation [13] is

$$\frac{\partial^2 \rho'}{\partial t^2} - c_0^2 \nabla^2 \rho' = \frac{\partial^2 T_{ij}}{\partial y_i \partial y_j} \tag{1}$$

where the Lighthill turbulence stress tensor, T_{ij}, is given by

$$T_{ij} = \rho V_i V_j + \delta_{ij}[(p - p_0) - c_0^2(\rho - \rho_0)] - \epsilon_{ij}\,. \tag{2}$$

Here ϵ_{ij} is the viscous stress tensor and, as is usual, it will be assumed that this term cam be safely ignored. For isothermal jets it is also reasonable to assume the usual baratropic relationship between pressure and density and this means that the second term on the right of the equation is identically zero. Consequently, the Lighthill tensor can be approximated as:

$$T_{ij} = \rho(U_i + u_i)(U_j + u_j)\,, \tag{3}$$

where the velocity field has been decomposed into a sum of mean and fluctuating components, $V_i = U_i + u_i$.

Since equation (1) is arrived at by a rearrangement of the full equations of motion it is necessarily exact. The right hand side therefore includes terms that should account for all the observed directivity effects arising from motion of the sources and the acoustic interaction with the mean flow. However as indicated in the introduction, the approach adopted in this paper is to account for these separately and a simpler source term that depends only on the turbulent velocity field will be considered. If mean flow effects are ignored equation (3) becomes

$$T_{ij} = \rho u_i u_j \tag{4}$$

where u_i is the fluctuating turbulent velocity.

In reality, this in a greater simplification than might at first appear. While it undoubtedly true that the presence of the mean velocity in the Lighthill source term must account for flow acoustic interaction effects, ignoring these terms entirely also eliminates the shear noise source terms. However, this is an assumption that is often made and is justified on the basis that the shear noise will scale with the self noise, as represented by the source given in equation (4). Substituting this into the right of equation (1) and changing from density to pressure fluctuations as the dependent variable, Lighthill's equation becomes:

$$\frac{1}{c_0^2}\frac{\partial^2 p}{\partial t^2} - \nabla^2 p = \frac{\partial^2 T_{ij}}{\partial y_i \partial y_j}\,, \tag{5}$$

where it will be understood that T_{ij} has the form given in equation (4). The solution is most easily found by using the free space Green's function that satisfies

$$\frac{1}{c_0^2}\frac{\partial^2 G^0}{\partial t^2} - \nabla^2 G^0 = -\delta(\mathbf{y}-\mathbf{x})\delta(\tau - t)\,, \tag{6}$$

and is given by

$$G^0(\mathbf{y},\tau|\mathbf{x},t) = \frac{1}{4\pi R}\delta(\tau - t + \frac{R}{c_0})\,, \tag{7}$$
$$R = |\mathbf{x}-\mathbf{y}|\,.$$

In terms of G^0, the solution to equation (5) can be formally written as

$$p(\mathbf{x},t) = \int_{-\infty}^{\infty}\iiint G^0(\mathbf{y},\tau|\mathbf{x},t)\frac{\partial^2 T_{ij}}{\partial y_i \partial y_j}\,d^3\mathbf{y}\,d\tau \tag{8}$$

where the spatial region will be taken over the entire source region.

Equation (8), with G^0 given by (7), is used in the analysis below as the starting point to obtain an explicit analytic form for the solution to Lighthill's equation. However, for future comparison with the solution to Lilley's equation, it is worthwhile pointing out that by means of two integrations by parts, equation (8) can be written as:

$$p(\mathbf{x},t) = \int_{-\infty}^{\infty}\iiint \frac{\partial^2 G^0}{\partial y_i \partial y_j}(\mathbf{y},\tau|\mathbf{x},t)T_{ij}\,d^3\mathbf{y}\,d\tau\,, \tag{9}$$

and by using equation (4) this has the explicit form

$$p(\mathbf{x},t) = \int_{-\infty}^{\infty}\iiint \frac{\partial^2 G^0}{\partial y_i \partial y_j}(\mathbf{y},\tau|\mathbf{x},t)\,\rho u_i u_j\,d^3\mathbf{y}\,d\tau\,. \tag{10}$$

Taking Fourier transforms we find the solution for

$$p_\omega(\mathbf{x}) = \int_{-\infty}^{\infty} p(\mathbf{x},t)e^{-i\omega t}\,dt \tag{11}$$

is given by

$$p_\omega(\mathbf{x}) = \iiint \frac{\partial^2 G^0_\omega(\mathbf{y}|\mathbf{x})}{\partial y_i \partial y_j}\,\rho(u_i u_j)^{FT}\,d^3\mathbf{y}\,, \tag{12}$$

where the superscript FT indicates the Fourier transform of the turbulent velocity product, and where

$$G^0_\omega(\mathbf{y}|\mathbf{x}) = \int_{-\infty}^{\infty} G^0(\mathbf{y},\tau|\mathbf{x},t)e^{i\omega(\tau-t)}\,dt\,, \tag{13}$$

is the reduced Green's function, (effectively the Fourier transform of the Green's function). It is given explicitly as:

$$G^0_\omega(\mathbf{y}|\mathbf{x}) = \frac{1}{4\pi R}e^{\frac{i\omega R}{c_0}}\,. \tag{14}$$

Needless-to-say, equations (8) and (12) are equivalent and will yield identical solutions if consistent assumptions and simplifications are made. Thus, when we later compare the formal

solution of Lilley's equation with equation (12) we recognise that this comparison applies also to to the solution resulting from equation (8) obtained below.

To continue with the Lighthill formalism, we now concentrate on finding a solution valid for the far-field where the observer is at a distance much greater than the maximum dimension of the source region. Using a coordinate system with origin at the jet nozzle, Figure 1, the approximation

$$R = |\mathbf{x} - \mathbf{y}| \approx |\mathbf{x}|$$

is valid in this region, and an expression for the far field pressure distribution can be obtained as (see for example, Goldstein [8]):

$$p(\mathbf{x}, t) = \frac{1}{4\pi c_0^2 x} \iiint \frac{\partial^2}{\partial t^2} T_{xx} \left(\mathbf{y}, t - \frac{|\mathbf{x} - \mathbf{y}|}{c_0} \right) d^3\mathbf{y} \,. \tag{15}$$

As before, the integral is taken over the entire jet volume, and T_{xx} is the component of the Lighthill stress tensor in the direction of the observer,

$$T_{xx} = \hat{x}_i \hat{x}_j T_{ij} \,.$$

Subsequent analysis yields an expression for the far field acoustic intensity spectrum as a double integral over the jet:

$$I_\omega(\mathbf{x}) = \frac{1}{32\pi^3 \rho_0 c_0^5} \frac{\omega^4}{x^2} \int \int R(\mathbf{y}, \boldsymbol{\eta}, \omega) e^{-i\omega \frac{\hat{\mathbf{x}} \cdot \boldsymbol{\eta}}{c_0}} \, d^3\boldsymbol{\eta} d^3\mathbf{y} \,. \tag{16}$$

Using overbars to denote time averages, R in this equation is defined as

$$R(\mathbf{y}, \boldsymbol{\eta}, \omega) = \int_{-\infty}^{+\infty} \overline{T_{xx}(\mathbf{y}, t) T_{xx}(\mathbf{y} + \boldsymbol{\eta}, t + \tau)} e^{-i\omega\tau} \, d\tau \;\; = \int_{-\infty}^{+\infty} R(\mathbf{y}, \boldsymbol{\eta}, \tau) e^{-i\omega\tau} \, d\tau \,, \tag{17}$$

and is the Fourier transform of the two-point correlation of the Lighthill stress tensor components in the direction of the far field observer:

$$R(\mathbf{y}, \boldsymbol{\eta}, \tau) = \overline{T_{xx}(\mathbf{y}, t) T_{xx}(\mathbf{y} + \boldsymbol{\eta}, t + \tau)}. \tag{18}$$

The inner integral of equation (16) can be interpreted as the integral over a locally correlated volume or eddy; while the outer integral sums all such contributions over the jet volume. (See Figure 1 for the coordinate system and definition of variables used in the calculations.) The functional form taken by $R(\mathbf{y}, \boldsymbol{\eta}, \omega)$ has been given by Self [24] as:

$$R(\mathbf{y}, \boldsymbol{\eta}, \omega) = \rho^2 u^4 \hat{R}(\mathbf{y}, \boldsymbol{\eta}, \omega) \tag{19}$$

where u is a velocity characteristic of the turbulence and $\hat{R}(\mathbf{y}, \boldsymbol{\eta}, \omega)$ is a "shape function" given by:

$$\begin{aligned} \hat{R}(\mathbf{y}, \boldsymbol{\eta}, \omega) = \;\; & 2\sqrt{\pi} \, \tau_s \exp\left\{ -\tfrac{\omega^2 (1 - M_c \cos\theta)^2 \tau_s^2}{4} \right\} \\ & \times \; \exp - \left\{ \tfrac{\eta_1^2}{l_1^2} + \tfrac{\eta_2^2}{l_2^2} + \tfrac{\eta_3^2}{l_3^2} \right\} . \end{aligned} \tag{20}$$

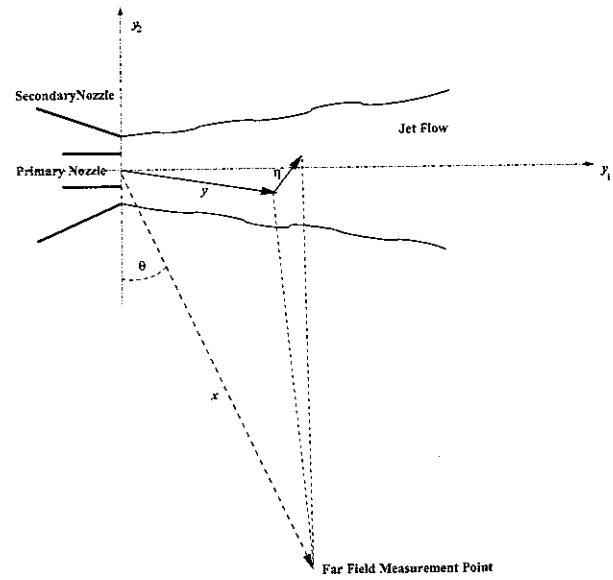

Figure 1: Coordinate system for the coaxial jet calculations

Here τ_s defines the moving axis timescale and is the characteristic time over which a turbulent eddy remains correlated; l_i are three lengthscales characterizing the size of the eddies. Defining U_c as the velocity with which eddies convect in the mean flow, the Mach number M_c is defined as $M_c = U_c/c_0$. For later use it is also useful to define moving axis lengthscale, $L_s = U_c\tau_s$, that characterizes the distance an eddy travels in the time τ_s due to its convection with velocity U_c. As stated, we allow these parameters to depend on frequency in a manner which will be discussed below.

The reason for modelling the spectral density directly (rather than modelling the correlation and taking the Fourier Transform) has been discussed in reference [24]. While the form given in equation (20) is superficially identical to that which would be obtained if the turbulence were modelled as Gaussian in a co-moving frame (which is an often made assumption), it is important to remember that the parameters in equation (20) are here assumed to be frequency dependent. In this case, an inverse Fourier Transform of $R(\mathbf{y}, \boldsymbol{\eta}, \omega)$ will not yield a correlation corresponding to convected Gaussian turbulence but will have a somewhat more complicated functional form. Physically the assumption being made is that the *filtered* correlations are Gaussian in nature, and this accords with the observations of Fisher and Davies[17]. (Although the measurements of these authors involved the turbulent velocities, it is not unreasonable to assume that the Reynold's stresses will be analogous.)

Substituting these expressions for $R(\mathbf{y}, \boldsymbol{\eta}, \omega)$ into (16) yields the final form for the far-field acoustic intensity spectrum which can be written as the integral of an equivalent acoustic source distribution, $q(\mathbf{y}, \omega)$, over the volume of the jet:

$$I_\omega(\mathbf{x}) = \frac{1}{32\pi^3\rho_0 c_0^5}\frac{\omega^4}{x^2}\int q(\mathbf{y},\omega)\, d^3\mathbf{y}. \tag{21}$$

The source distribution, $q((\mathbf{y},\omega)$, is found to be given by

$$q(\mathbf{y},\omega) = 2\pi^2\rho^2 l_{||} l_{\perp}^2 \tau_s u^4 \exp\left\{-\frac{\omega^2(l_{||}^2\cos^2\theta + l_{\perp}^2\sin^2\theta)}{4c_0^2}\right\} \times \exp\left\{-\omega^2(1-M_c\cos\theta)^2\tau_s^2\right\} \quad (22)$$

where $l_{||} = l_1$ is the axial lengthscale. We take the transverse lengthscales, l_2 and l_3, as equal

$$l_2 = l_3 = l_{\perp}\,. \quad (23)$$

An obvious assumption to make at this point is that the turbulence is isotropic, *i.e.*

$$l_{||} = l_{\perp}\,, \quad (24)$$

this being so because a k-ϵ turbulence model yields only one lengthscale. However, it is well known that this is untrue for jet flows where the directionality of the mean flow tends to "stretch" the turbulent eddies. This effect will be stronger nearer the nozzle where the mean velocity field is most intense and we would expect that a more appropriate relationship would be

$$l_{||} = f(\mathbf{y})l_{\perp} \quad (25)$$

where the $f(\mathbf{y})$ accounts for the variation in eddy aspect ratio as it convects downstream.

3 Relationship of the acoustic source model to the RANS output

It is necessary to consider how the various parameters in equation (22) for $q(\mathbf{y},\omega)$ relate to RANS derived quantities and how they vary with frequency; the moving axis timescale, τ_s being crucially important. If $\tau_s \rightarrow \infty$ then the turbulence becomes "frozen", and no noise will be produced [17]. As τ_s decreases, the turbulence decays more quickly as it convects downstream, and the noise production mechanisms are enhanced. For a single stream jet, the author [24] proposed a variation with frequency for the moving-axis lengthscale as

$$\frac{L_s}{W} = \frac{c_1}{(1+\omega/\omega_c)}, \tag{26}$$

that can be written in terms of τ_s as:

$$\tau_s = \frac{c_1 W}{U_c(1+\omega/\omega_c)}. \tag{27}$$

In both cases where

$$\omega_c = 2\pi c_2 U_1/W, \tag{28}$$

and c_1 and c_2 are constants. W is the local shear layer width, and U_1 is the centreline jet velocity.

These relationships are a consistent generalization which fit the measurements made by Harper-Bourne [9] and represent a universal scaling with a local Strouhal number $St = \omega W/U_1$, defined in terms of U_1 and W, but there is also an implicit assumption that the moving axis timescale is a function only of frequency and axial position in the jet, $\tau_s = \tau_s(y_1,\omega)$.In reality $u(\mathbf{y})$ varies radially as well as axially, but the well known similarity laws obeyed by single stream jet flows means it is permissible to take a single value of τ_s as being characteristic of the shear layer as a whole. This is not possible for coaxial jets where the presence of two shear layers and the consequent complexity of the flow field requires that the relationships be given in terms of locally defined variables. This is easily accomplished by recognising that U_1/W is a measure of the mean shear rate and proposing the local equivalent. Also, because we expect the local turbulence intensity u/U to be proportional to the shear rate we are able to write the relationships in terms of the RANS derived turbulent kinetic energy, k. Whereas previously the acoustic lengthscale $l_\perp$ was taken as proportional to the shear layer width, W, a natural generalisation is to assume a proportional dependence on the RANS lengthscale, l_{CFD}, defined in the k-ϵ model by $l_{CFD} = k^{3/2}/\epsilon$. The complete list of relationships needed to evaluate (22) and integrate equation (21) is taken as:

$$u = \sqrt{\frac{2k}{3}}, \qquad U_c = U. \tag{29}$$

$$l_\perp = c_l \frac{\sqrt{k^3}}{\epsilon}, \qquad l_{||} = l_\perp. \tag{30}$$

$$\tau_s = \frac{c_\tau}{\omega+\omega_c}, \qquad \omega_c = c_\omega \frac{U}{\sqrt{2k/3}}. \tag{31}$$

4 Lilley's Analogy and the directivity model

The noise produced by jets shows a marked directivity, and as discussed in the introduction, this arises for a number of reasons. Two effects are apparent in equation (22) in the angular dependence of the arguments of the exponentials. The first of these will not be manifested in the present analysis because we have taken the assumption of isotropy (equation 24). It will only arise when an anisotropic turbulence model is used — either via an *ad hoc* assumption such as (25) or by using a more sophisticated CFD model that gives more than one lengthscale (for example a Reynold's Averaged code). Because turbulent jet flows are anisotropic this may represent a source of error for high frequency noise that originates mainly from the region of the jet flow close to the nozzle where the mean flow is high, but will be less so for low frequencies that mainly originate further downstream where the mean flow is less intensive.

The angular dependence of the argument in the second exponential in equation (22) is a retarded time effect and arises from the necessary delay in transmission times if noise from different parts of a non-compact eddy convecting in the mean flow is to arrive simultaneously at the observer.

A third source of directivity arises, however, from the effects of flow-acoustic interaction as the acoustic waves propagate through the shear layer. Since Lighthill's Analogy assumes that the acoustic sources are situated in homogeneous medium at rest, as manifested by the use of the free space Green's function in equation (8), it is not possible to incorporate such effects consistently within the Lighthill formalism. Rather, we must seek a formalism that recognises from the outset that the acoustic sources are convected by the mean flow and that the noise they produce must propagate through this (varying) mean flow before reaching the ambient medium and finally the far-field observer.

A suitable form of the Acoustic Analogy for the present analysis has been given by Lilley [15]. In the case of axisymmetric circular jet with transversely sheared mean flow ($\mathbf{U} = U\hat{\mathbf{i}}$) Lilley's convected wave equation can be written as [8]

$$L(\Pi) \equiv \frac{D}{Dt}\left(\frac{D^2}{Dt^2} - \nabla \cdot c_0^2 \nabla\right)\Pi + 2c_0^2 \frac{dU}{dr}\frac{\partial^2 \Pi}{\partial y_1 \partial r} = \frac{D}{Dt}\frac{\partial^2 u_i u_j}{\partial y_i \partial y_j} - 2\frac{dU}{dr}\nabla r \cdot \frac{\partial^2 \mathbf{u} u_i}{\partial y_1 \partial y_i}. \tag{32}$$

The convected derivative appearing in this equation is defined with respect to the mean velocity of the flow:

$$\frac{D}{Dt} \equiv \frac{\partial}{\partial t} + U\frac{\partial}{\partial y_1} \tag{33}$$

and y_1 is the axial coordinate to which the mean flow is assumed parallel. The transverse radial variable r is defined as

$$r = \sqrt{y_2^2 + y_3^2},$$

and the dependent variable,

$$\Pi = \frac{1}{\gamma}\ln\left(\frac{p_0 + p}{p_0}\right) \tag{34}$$

is essentially the pressure fluctuation p normalised by $c_0^2\rho_0$:

$$\Pi \sim \frac{p}{c_0^2 \rho}. \tag{35}$$

As with Lighthill's equation we can formally solve (32) by introducing a Green's function $g(\mathbf{x}, t|\mathbf{y}, \tau)$ that satisfies

$$L(g) = c_0^2 \delta(\mathbf{x} - \mathbf{y})\delta(t - \tau)\,, \tag{36}$$

to give using (35):

$$p = \rho \int_{-\infty}^{\infty} \iiint g(\mathbf{y}, \tau|\mathbf{x}, t) Q \, d^3\mathbf{y} \, d\tau\,, \tag{37}$$

where Q represents the source terms on the right hand side of equation (32). We recognise the first of these terms as equivalent to the self noise source used in the Lighthill formalism above. Since the Lilley equation now includes all the propagation effects within the convected wave operator on the left of the equation, the second term making up Q must represent the shear noise source. If we are willing to accept (as was done above) that a sufficiently accurate estimate of the far-field noise can be made by ignoring this term then matters are greatly simplified. Taking

$$Q \approx \frac{D}{Dt} \frac{\partial^2 u_i u_j}{\partial y_i \partial y_j}\,, \tag{38}$$

we recognise that the integrand on the right of equation (37) is the product of the Green's function with the convected derivative of a pure divergence and we are able to apply Green's theorem to give:

$$p(\mathbf{x}, t) = \int_{-\infty}^{\infty} \iiint \frac{\partial^2 G}{\partial y_i \partial y_j}(\mathbf{y}, \tau|\mathbf{x}, t) \rho u_i u_j \, d^3\mathbf{y} \, d\tau\,, \tag{39}$$

where the convected derivative of the Green's function

$$G = \frac{Dg}{D\tau}\,, \tag{40}$$

satisfies

$$L(G) = c_0^2 \frac{D}{D\tau} \delta(\mathbf{x} - \mathbf{y})\delta(t - \tau)\,. \tag{41}$$

Rather than dealing directly with $G(\mathbf{y}, \tau|\mathbf{x}, t)$ it is advantageous to take Fourier transforms:

$$p_\omega(\mathbf{x}) = \int_{-\infty}^{\infty} p(\mathbf{x}, t) e^{-i\omega t} \, dt\,, \tag{42}$$

$$G_\omega(\mathbf{y}|\mathbf{x}) = \int_{-\infty}^{\infty} G(\mathbf{y}, \tau|\mathbf{x}, t) e^{i\omega(\tau - t)} \, dt\,, \tag{43}$$

to give the formal solution

$$p_\omega(\mathbf{x}) = \iiint \frac{\partial^2 G_\omega(\mathbf{y}|\mathbf{x})}{\partial y_i \partial y_j} \rho(u_i u_j)^{FT} \, d^3\mathbf{y}\,, \tag{44}$$

where the superscript FT again indicates the Fourier transform of the argument.

Comparing equations (39) and (44) with the corresponding equations obtained in the Lighthill formalism, equations (10) and (12), it is immediately apparent that they differ only to the extent that the Green's functions differ from one another. We therefore anticipate that if we are able to write the Lilley equation Green's function as a product of free space Green's

function and a modifying factor we will also be able to account for the flow acoustic directivity effects by modifying the Lighthill solution obtained above by a suitable flow factor. To this end we note that in cylindrical coordinates:

$$(\, y_1,\, r = \sqrt{y_2^2 + y_3^2},\, \phi = \cos^{-1}\frac{y_2}{r}\,)$$

G_ω can be decomposed as the sum:

$$G_\omega(\mathbf{y}|\mathbf{x}) = \frac{1}{4\pi^2}\Sigma_{n=-\infty}^{\infty} e^{in\Delta\phi} \int_{-\infty}^{\infty} G_n(r_s|r;\omega,k_1)e^{ik_1(x_1-y_1)}\,dk_1 \tag{45}$$

where $\Delta\phi = \phi_{\mathbf{x}} - \phi_{\mathbf{y}}$ is the difference in the azimuthal coordinates of observer and source positions. The equations equivalent to (41) satisfied by the G_n's are

$$\Phi^2\frac{d}{dr}\left(\frac{r}{\Phi^2}\frac{dG_n}{dr}\right) + \left(1 - \frac{\kappa^2}{\Phi^2}\right)k_0^2r^2G_n - \frac{n^2}{\Phi^2}G_n = -\delta(r_{\mathbf{x}} - r_{\mathbf{y}})\,, \tag{46}$$

where

$$k_0 = \omega/c_0, \qquad \kappa = k_1/k_0, \qquad M(r) = U(r)/c_0, \qquad \Phi = 1 - \kappa M(r), \tag{47}$$

and where r is understood as being evaluated at $\mathbf{x}$ and variables carrying a subscript s are understood as being evaluated at the source position $\mathbf{y}$.

This set of ordinary differential equations is clearly more amenable to solution than a partial differential equation and following the method given in [19] a solution to (46) can be written as

$$\begin{aligned} G_n(r_s|r) &= \frac{p_i(r)p_o(r_s)}{r_s\Delta(r_s)} \qquad r < r_s \\ &= \frac{p_o(r)p_i(r_s)}{r_s\Delta(r_s)} \qquad r > r_s \end{aligned} \tag{48}$$

where p_i and p_o are two independent solutions to the corresponding homogeneous equation and Δ is their Wronskian:

$$\Delta(r) = p_i(r)\frac{dp_o(r)}{dr} - \frac{dp_i(r)}{dr}p_o(r)\,.$$

While it does not appear possible to find a closed form analytic solution for p_i and p_o, it is evident that we can determine their asymptotic form as $r \to 0$ and $r \to \infty$ respectively. In each of these limits the homogeneous equivalent of equation (46) satisfied by p_i and p_o approaches a Bessel equation and we can write

$$p_i(r) \sim \mathrm{J}_n(\kappa_J r) \qquad r \to 0\,, \tag{49}$$

as the ingoing solution that is finite on the jet centreline and

$$p_o(r) \sim \mathrm{H}_n^{(2)}(\kappa_\infty r) \qquad r \to \infty\,, \tag{50}$$

as the outgoing wave solution.

More generally, we can find approximate solutions for p_i and p_o, and hence G_n, in the low and high frequency asymptotic regimes. The applicability of these asymptotic solutions is discussed in more detail later, but for the present we can (somewhat loosely) define them as being given by the limits $r_J k_0 \to 0$ and $r_J k_0 \to \infty$ respectively where r_J is the nozzle diameter that can be taken a characteristic lengthscale in the source region and which is naturally used to non-dimensionalise k_0.

Low frequency solution

We begin by considering the low frequency limit where there are two separate solution regions for equation (46) depending on whether $r \sim r_J$ or $r \sim k_0^{-1}$. In the first case the second term can be safely ignored by virtue of the distinguished limit $r_J k_0 \to 0$ and p_i and p_o will satisfy the equation

$$\frac{d}{dr}\left(\frac{r}{\Phi^2}\frac{dp}{dr}\right) = -\frac{n^2}{\Phi^2}p\,. \tag{51}$$

For low frequencies jet noise is dominated by the low azimuthal modes [28] and we will assume that the behaviour of these solutions is similar to that of the $n = 0$ mode. Putting $n = 0$ in equation (51) we immediately obtain the solutions:

$$p_i(r) = \text{constant} \tag{52}$$

$$p_o(r) = A\int \frac{\Phi^2(r)}{r}dr \tag{53}$$

and where

$$p_o(r)A \sim \ln r \qquad \text{as} \qquad r \to \infty\,. \tag{54}$$

The significance of (54) is that p_o as given by equation (53) will not have the correct asymptotic form (as given by equation 50) in the far field, and must therefore represent an *inner* solution. The corresponding *outer* solution will be found by solving in the $r \sim k_0^{-1}$ case. An arbitrary constant A has been included in equation (53) to facilitate matching of the inner and outer solutions.

For the outer solution the second term in equation (46) can no longer be ignored because we now have $k_0 r \sim O(1)$. However, because the mean velocity is monotonically decreasing to zero as $r \to \infty$ we can form an approximation by taking $\Phi \sim 0$ and the equation for p_i and p_o is now a Bessel equation that, for $n = 0$ will give the solution

$$p_o(r) = H_0^{(1)}(rk_0\sqrt{1-\kappa^2})\,, \tag{55}$$

and this has asymptotic behaviour $H_0^{(1)}(rk_0\sqrt{1-\kappa^2}) \sim (2i/\pi)\ln r$ as $k_0 r \to 0$. If the inner and outer solutions are to match, we must clearly take $A = (2i/\pi)$, and for a far field solution the composite solutions for p_i and p_o will be given by equations (52) and (55) respectively.

The Wronskian $\Delta(r_s)$ is now easily found, and substituting the second of equations (48) and using the large argument approximation to $H_0^{(1)}$ we find that

$$G_0(r|r_s) \sim \sqrt{\frac{i\pi}{2k_0 r}}\frac{e^{irk_0\sqrt{1-\kappa^2}}}{\Phi^2(r_s)(1-\kappa^2)^{1/4}}\,, \qquad k_0 r_J \to 0, k_0 r \to \infty\,. \tag{56}$$

To determine G_ω it is useful to introduce a polar coordinate system defined by

$$\begin{aligned} R &= \sqrt{(r-r_s)^2+(x_1-y_{1s})^2} \\ \theta &= \cos^{-1}\frac{x_1-y_{1s}}{R} \end{aligned} \tag{57}$$

and where we recognise θ as the angle of the far field observer from the jet axis. Substituting into equation (45) and obtaining the integral as an asymptotic approximation for large $k_0 r$ [3] gives:

$$G_\omega(\mathbf{y}|\mathbf{x}) \sim \frac{G^0_\omega(\mathbf{y}|\mathbf{x})}{(1-M(r_s)\cos\theta)^2}\,. \tag{58}$$

High frequency solution

We now consider the high frequency limit, $k_0 r_J \to \infty$ and start by putting equation (46) into Sturm-Liouville form by making the change of dependent variable

$$\overline{p}_{i,o}(r) = \frac{\Phi(r)}{r^{1/2}} p_{i,o}(r)$$

to give

$$\frac{d^2\overline{p}}{dr^2} + (k_0^2 q_n(r) + s(r))\overline{p} = 0\,, \tag{59}$$

where

$$q_n = \Phi^2 - \kappa^2 - \frac{n^2}{k_0^2 r^2} \tag{60}$$

$$= q^2 - -\frac{n^2}{k_0^2 r^2}\,, \qquad \text{where} \qquad q^2 = \Phi^2 - \kappa^2 \tag{61}$$

and where

$$s(r) = \frac{\Phi}{r}\frac{d}{dr}\left(\frac{r}{\Phi^2}\frac{d\Phi}{dr}\right) + \frac{1}{4r^2}\,.$$

We also note that, using the polar coordinates defined in (57), $q^2 = \Phi^2 - \cos^2\theta$.

As is well known, determining the high frequency approximation to a Sturm-Liouville problem depends upon the turning points of the equation that, for (59), are given by the zeros of $q_n(r)$. We will assume that $q_n(r)$ has only one zero that occurs a $r = r_T$ that we will refer to as the *transition point*. Using the standard WKB methodology [19] we can obtain two independent asymptotic solutions to equation (59) in terms of Hankel functions as done by Goldstein [8]:

$$\overline{p}_i = A\frac{\xi^{3/4}}{q_n^{1/4}} H^{(1)}_{1/3}\left(\frac{2}{3}k_0\xi^{3/2}\right) \tag{62}$$

$$\overline{p}_o = A\frac{\xi^{3/4}}{q_n^{1/4}} H^{(2)}_{1/3}\left(\frac{2}{3}k_0\xi^{3/2}\right) \tag{63}$$

where

$$\xi = \left\{ \frac{3}{2} \int_{r_T}^{r} \sqrt{\pm q_n(t)}\, dt \right\}^{2/3} \tag{64}$$

where $+q_n$ is taken for $r > r_T$ and $-q_n$ for $r < r_T$, and to match with known aysmptotic behaviour (50) we must take $A = \sqrt{(k_0\pi)/3}$. Expanding the Hankel functions for the far-field $r \to \infty$ gives:

$$\overline{p}_i \sim \frac{1}{q_n(r)^{1/4}} e^{ik_0 \int_{r_s}^{r} \sqrt{q_n(r)}\, dr}, \tag{65}$$

$$\overline{p}_o \sim \frac{1}{q_n(r)^{1/4}} e^{-ik_0 \int_{r_s}^{r} \sqrt{q_n(r)}\, dr}. \tag{66}$$

Using these to determine p_i, p_o and the Wronskian Δ it is a straightforward matter to show that G_ω will be given by

$$G_\omega \sim \frac{1}{4\pi^2} \Sigma_{n=-\infty}^{\infty} e^{in\Delta\phi} \frac{i}{2k_0} \frac{1}{\sqrt{r r_s}} \int_{-\infty}^{\infty} \frac{e^{ik_0 \int_{r_s}^{r} \sqrt{q_n(r)} dr}}{\Phi(r_s)(1-\kappa^2)^{1/4} q_n(r_s)^{1/4}}\, dk_1 \tag{67}$$

Writing the integrals in terms of the polar coordinates (57) and, as with equation (58) using an asymptotic approximation for large $k_0 r$, we find G_ω can be written as

$$G_\omega \sim \frac{G_\omega^0(\mathbf{y}|\mathbf{x}) R_\omega(\mathbf{y}|\mathbf{x})}{(1 - M(r_s)\cos\theta)}, \tag{68}$$

where

$$R_\omega(\mathbf{y}|\mathbf{x}) = -\left(\frac{i}{2\pi r_s k_0}\right)^{1/2} \Sigma_{n=-\infty}^{\infty} \frac{e^{in\Delta\phi + ik_0 \int_{r_s}^{r} Q_n(r) dr}}{Q_n(r_s)^{1/2}} \tag{69}$$

where Q_n is defined by

$$Q_n(r) = \sqrt{(1 - M(r)\cos\theta)^2 - \cos^2\theta - (n/k_0 r)^2}. \tag{70}$$

So long as Q_n is real, the integral in the argument of the exponential of equation (68) will only effect the relative phasing of the modes. If, on the other hand, Q_n is imaginary then the exponential will contain a real argument that leads to exponential damping of the sound, and this occurs when θ lies within the so-called *cone of silence* defined by the angle θ_0 where

$$\cos\theta_0 = \frac{1}{1 + M(r_s)} \tag{71}$$

and which indicates that angle where a simple analysis based on Snell's law would predict total internal reflection to occur. Within this region the the sound will suffer an amount of damping given by

$$e^{-k_0 \int_{r_s}^{r_T} |Q_n(r)| dr}. \tag{72}$$

By assuming that we can approximate the integrand $|Q_n(r)|$ in equation (72) by $|Q_{n=0}|$ a unique exponential decay factor is defined for each source position that can be calculated by numerical integration.

In this section we have derived expressions that show how the far-field pressure is affected by the presence of the flow, and equations (58) and (68) indicate that we can obtain the with-flow solution by applying a multiplicative factor to the elementary solutions of the no-flow problem before integrating over the source region. In the previous section an expression for the far-field acoustic *intensity* with no-flow was given so clearly we must use the square of pressure factor in this case. We will refer to this factor as a *Flow Factor* defined as

$$F(\omega,\theta) = \frac{1}{(1-M(r_s)\cos\theta)^4} \qquad k_0 r_J \to 0, \qquad r \to \infty\,, \tag{73}$$

$$= \frac{|R|^2}{(1-M(r_s)\cos\theta)^2} \qquad k_0 r_J \to \infty\,, \tag{74}$$

with R be given by the sum above.

5 The combined prediction scheme

The prediction for the far-field noise spectra of a given jet flow is now obtained by combining the source model given in equation (22) with the appropriate Flow Factor given by equation 73) for the low frequency case and equation 74) for the high frequency case to yield:

$$I_\omega(\mathbf{x}) = \frac{1}{32\pi^3\rho_0 c_0^5}\frac{\omega^4}{x^2}\int_{V_{jet}} F(\omega,\theta)q(\mathbf{y},\omega)\,d^3\mathbf{y}. \tag{75}$$

In this expression the integral is taken over the full 3-d region of the CFD predicted flow. The various terms in (75) are evaluated using their relationship with the CFD data provided by equations (29 – 30).

Because the jets considered are assumed axisymmetric we can write equation (75) in cylindrical coordinates as:

$$I_\omega(\mathbf{x}) = \frac{1}{16\pi^2\rho_0 c_0^5}\frac{\omega^4}{x^2}\int_0^\infty\int_0^\infty rF(\omega,\theta)q(r,x,\omega)\,drdx\,, \tag{76}$$

(r being the radial coordinate from the jet axis, and x the distance along that axis from the nozzle), and this gives an immediate expression for the axial source strength distribution. We can think of this as an equivalent line distribution of sources $q(x,\omega)$ that would give the same far-field spectra. As seen from 90 degrees to the jet axis $q(x,\omega)$ is given by

$$q(x,\omega) = \frac{\omega^4}{16\pi^2\rho_0 c_0^5}\int_0^\infty rq(r,x,\omega=\pi/2)\,dr\,, \tag{77}$$

where we have used the fact that both the convective directivity and the flow factor are unity for propagation perpendicular to the jet axis. The predicted source distribution can be compared to measured source distributions as a useful check on the theory.

However, it still remains to determine the limits of the high and low frequency solutions and which of the two asymptotic expressions (73), (74) to use. In the results obtained below we have taken the pragmatic step of assuming that the high frequency Flow Factor (74) applies whenever we are *inside* the cone of silence and that the low frequency Flow Factor (73) applies outside.

6 CFD prediction of the flow field

The CFD data used in the current study were provided by Gary Page and Jim McGuirk of Loughborough University — see reference[21]. The CFD methodology solved the compressible Reynolds Averaged Navier Stokes equations using a $k-\epsilon$ model coupled with appropriate wall-functions for turbulence closure. The methodology was validated by comparison with Laser Doppler Velocimetry measurements[20].

CFD calculations were made for two co-planar coaxial nozzles with ratio of secondary nozzle are to primary nozzle area of $A_s/A_p = 2$ and $A_s/A_p = 4$. In each case two velocity ratios were computed corresponding to a (nominal) ratio of secondary nozzle flow velocity to primary nozzle flow velocity of $V_s/V_p = 0.6$ and $V_s/V_p = 0.8$. The nozzle geometries and flow conditions represent those used for the experimental measurements on a set of small scale nozzles and described below. In each of the two cases the primary nozzle diameter was set at $33mm$ and the secondary flow velocity at $V_s = 170m/s$.

The CFD predictions were processed to produce mean velocity, length scale and turbulence intensity (expressed as $(\sqrt{2k/3}/V_p) \times 100\%$) that were used as input to the noise calculations and defined at positions $(x/D, r/D)$ in the and assuming axial symmetry.

7 Overview of Results

In order to utilise the CFD data in the noise model the various parameters defined in equations (29), (30) and (31) need to be determined. Their values were decided by overall best fit to the 90° spectra of the four different coaxial configurations considered. It was found that a reasonable fit to the measured spectrum was obtained by using the values,

$$c_\tau = 5.75, \quad c_\omega = 8.4, \quad c_l = 0.75, \tag{78}$$

and these values were used for all the subsequent coaxial jet predictions regardless of observer angle.

As described below, the predicted spectra have been compared with experimental far field acoustic measurements made at QinetiQ's Noise Test Facility, Pyestock, UK. The far field SPL spectra were obtained in 1/3 octave bands (centre frequencies in the range 250 Hz to 40 kHz and corrected for atmospheric attenuation and re-scaled to a nominal distance of 6 m from the jet nozzle.

At the same time as the spectral measurements were made, a polar array of microphones was used to measure the axial source distribution of each of the jets[2]. The predicted source distributions have been compared with these.

Finally, far field spectra have been computed using a pre-existing semi-empirical method based on the Four Source Model[6, 7]. This also provides some limited information about the strength and distribution of the source densities, and the predictions from the current model compared to these.

8 Comparison of calculated and measured spectra

The far field intensity spectra was computed for each of the four test conditions at a distance of $6m$ from the nozzle and at a number of observation angles. These ranged from 30° to the downstream axis to 120° to the axis. These results are compared below to the measured data.

8.1 Area ratio 2, Velocity ratio 0.6 spectra comparisons

The comparisons for an area ratio 2 jet with a velocity ratio of 0.6 are shown in Figure 2 (a)–(j) below.

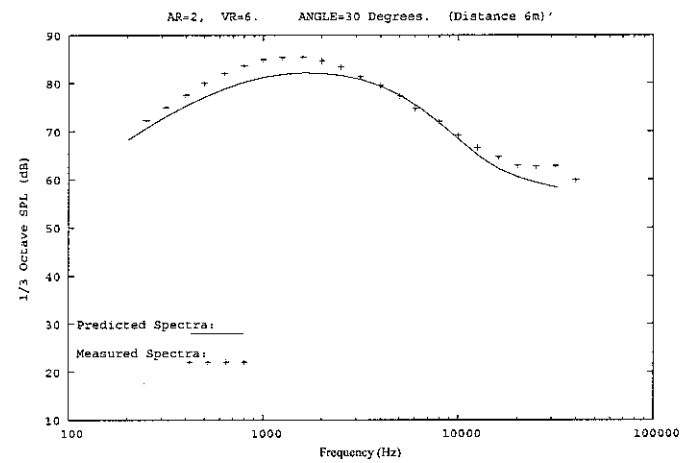

(a) Spectrum at 30° to jet axis.

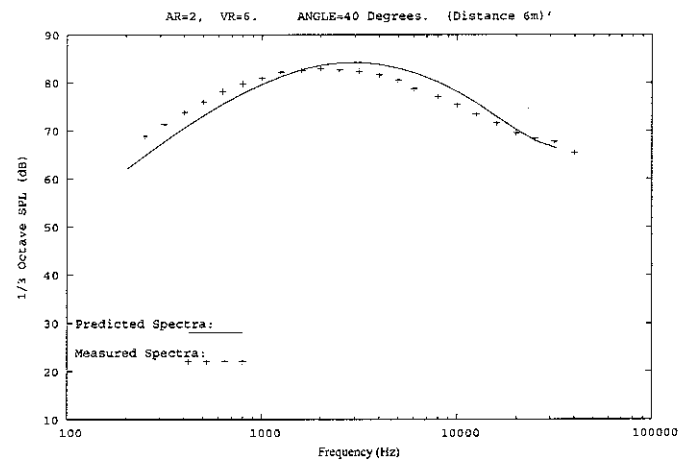

(b) Spectrum at 40° to jet axis.

Figure 2: Spectra for an Area Ratio 2, Velocity Ratio 0.6 Jet at various angles to the jet axis.

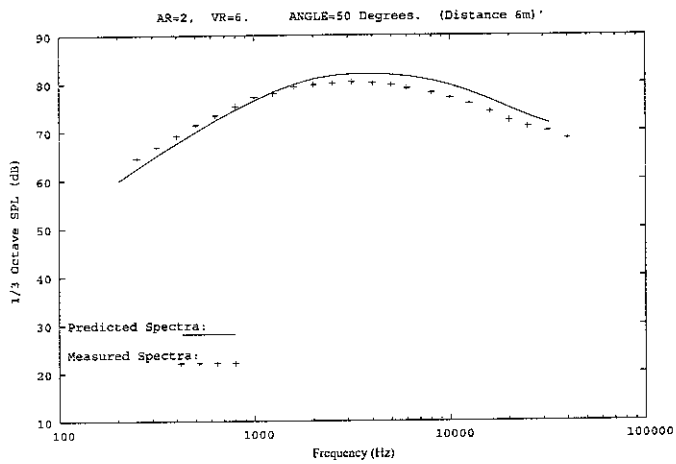

(c) Spectrum at 50° to jet axis.

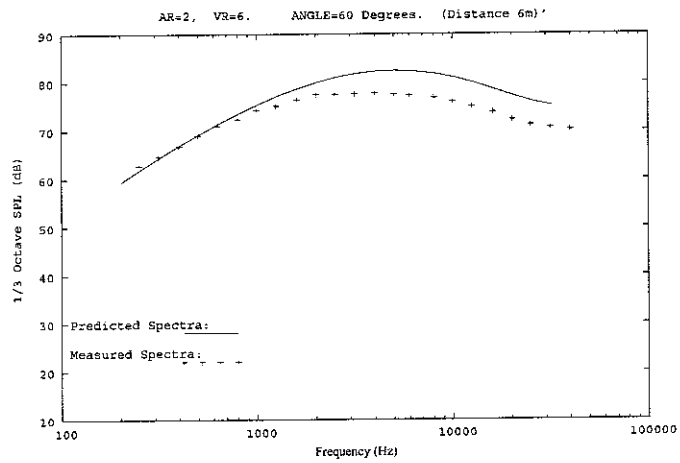

(d) Spectrum at 60° to jet axis.

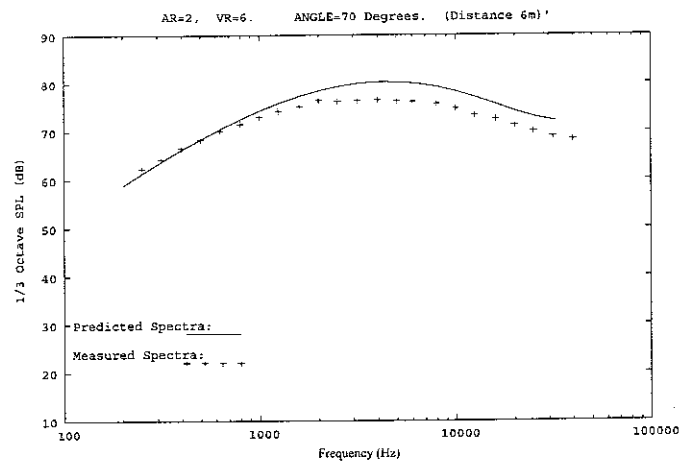

(e) Spectrum at 70° to jet axis.

Figure 2: (Contd.) Spectra for an Area Ratio 2, Velocity Ratio 0.6 Jet at various angles to the jet axis.

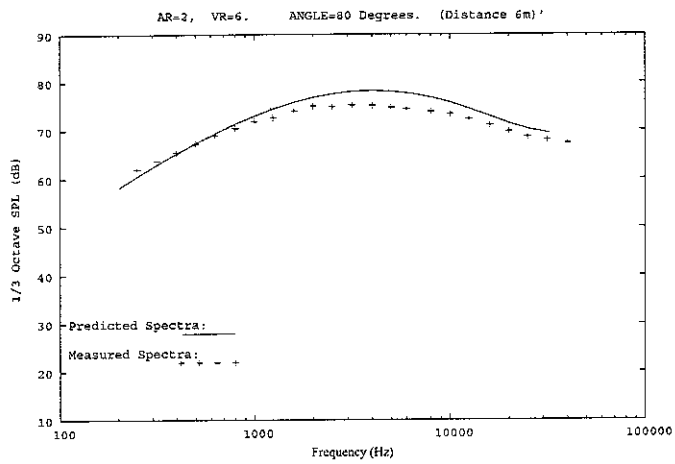

(f) Spectrum at 80° to jet axis.

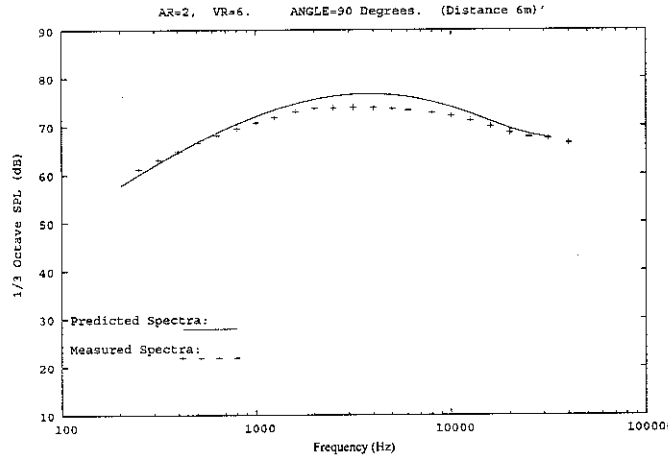

(g) Spectrum at 90° to jet axis.

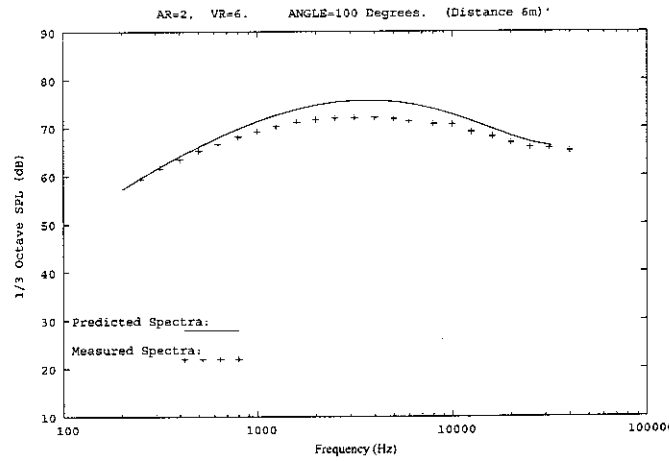

(h) Spectrum at 100° to jet axis.

Figure 2: (Contd.) Spectra for an Area Ratio 2, Velocity Ratio 0.6 Jet at various angles to the jet axis.

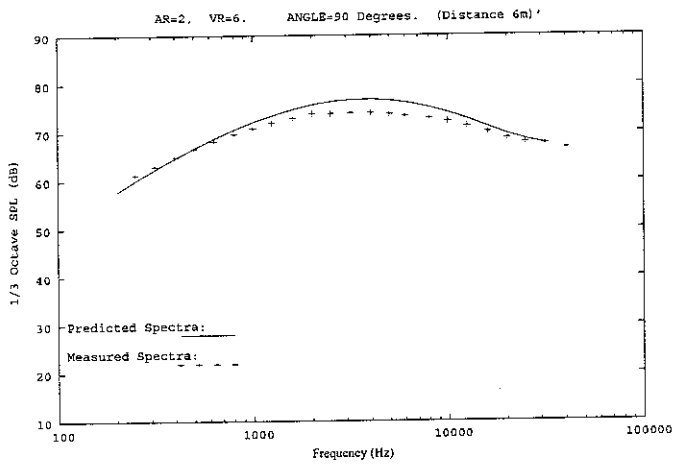

(i) Spectrum at 110° to jet axis.

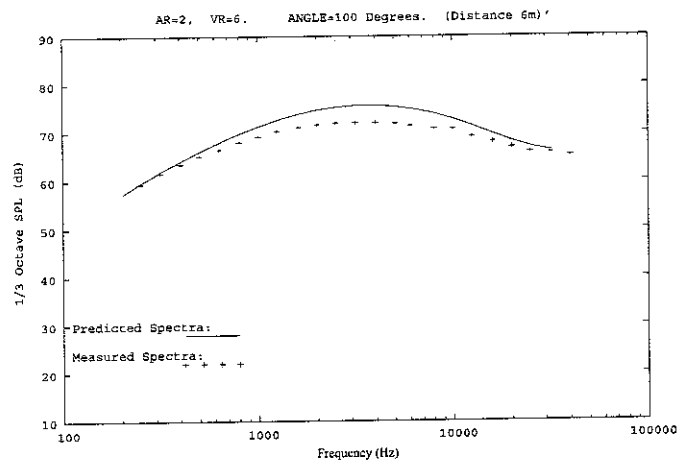

(j) Spectrum at 120° to jet axis.

Figure 2: (Contd.) Spectra for an Area Ratio 2, Velocity Ratio 0.6 Jet at various angles to the jet axis.

8.2 Area ratio 2, Velocity ratio 0.8 spectra comparisons

The comparisons for an area ratio 2 jet with a velocity ratio of 0.8 are shown in Figure 3 (a)–(j) below.

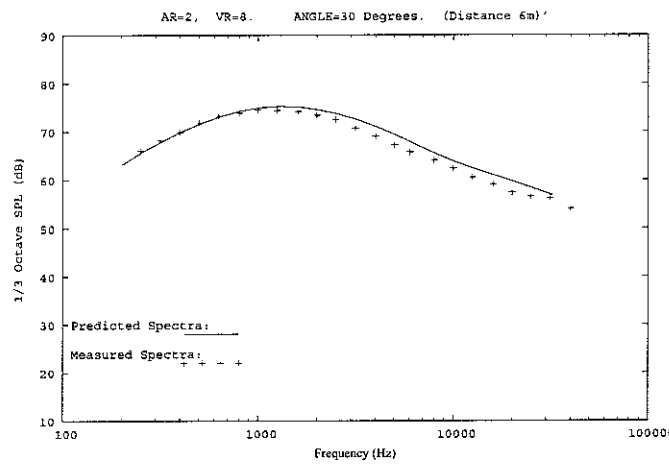

(a) Spectrum at 30° to jet axis.

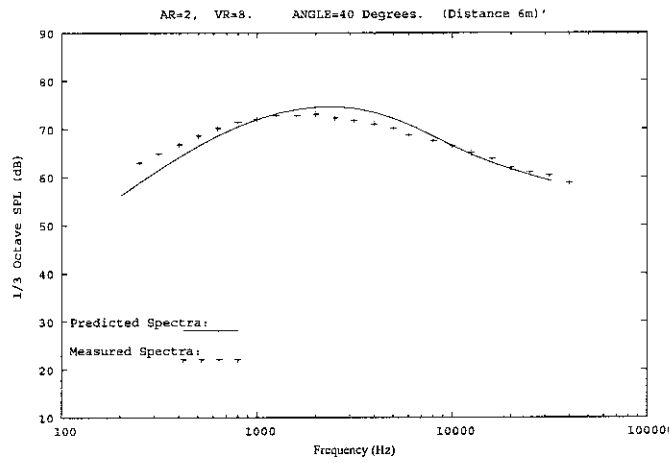

(b) Spectrum at 40° to jet axis.

Figure 3: Spectra for an Area Ratio 2, Velocity Ratio 0.8 Jet at various angles to the jet axis.

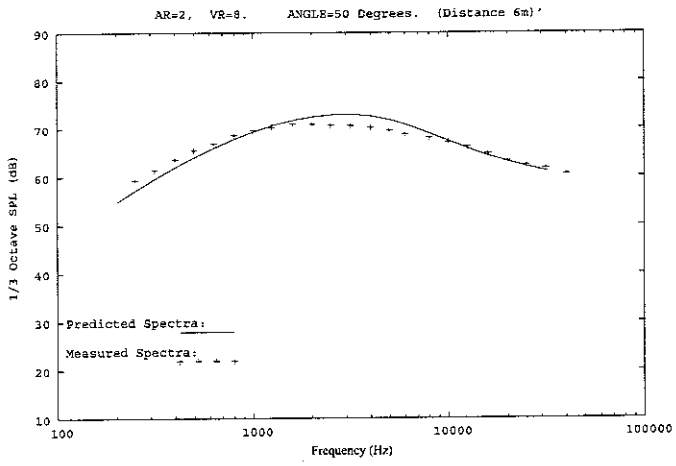

(c) Spectrum at 50° to jet axis.

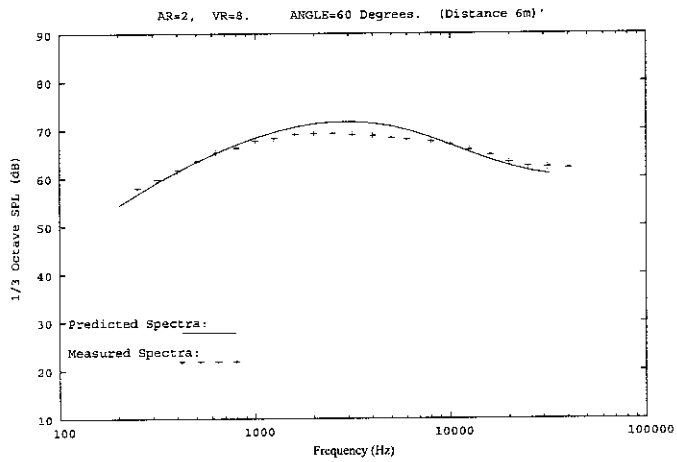

(d) Spectrum at 60° to jet axis.

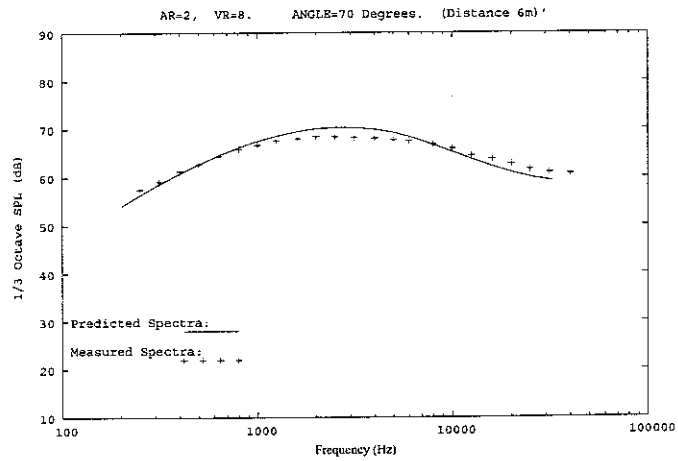

(e) Spectrum at 70° to jet axis.

Figure 3: (Contd.) Spectra for an Area Ratio 2, Velocity Ratio 0.8 Jet at various angles to the jet axis.

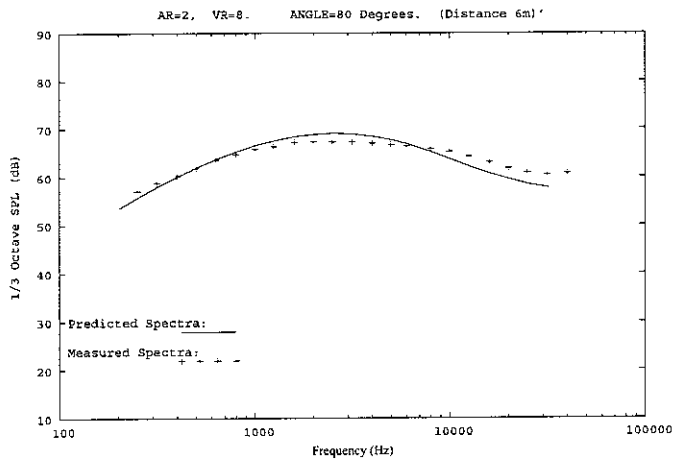

(f) Spectrum at 80° to jet axis.

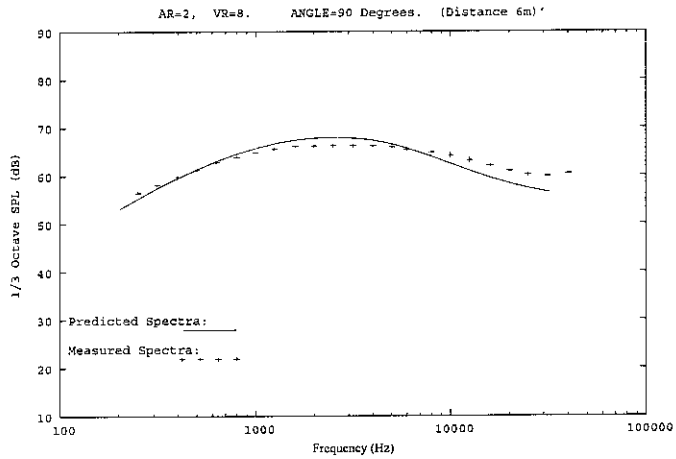

(g) Spectrum at 90° to jet axis.

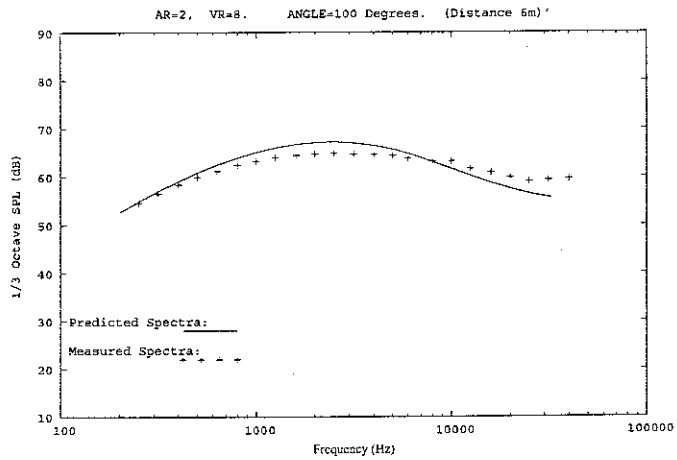

(h) Spectrum at 100° to jet axis.

Figure 3: (Contd.) Spectra for an Area Ratio 2, Velocity Ratio 0.8 Jet at various angles to the jet axis.

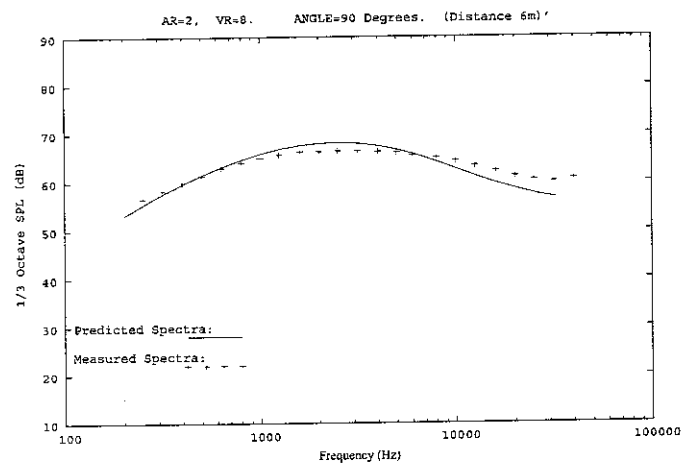

(i) Spectrum at 110° to jet axis.

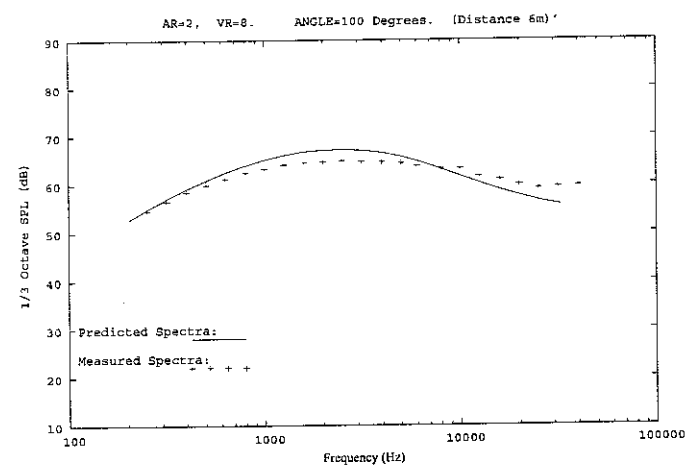

(j) Spectrum at 120° to jet axis.

Figure 3: (Contd.) Spectra for an Area Ratio 2, Velocity Ratio 0.8 Jet at various angles to the jet axis.

8.3 Area ratio 4, Velocity ratio 0.6 spectra comparisons

The comparisons for an area ratio 2 jet with a velocity ratio of 0.6 are shown in Figure 4 (a)–(j) below.

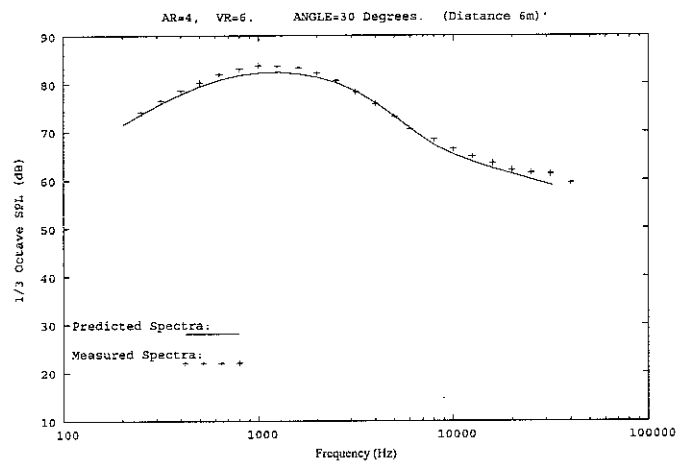

(a) Spectrum at 30° to jet axis.

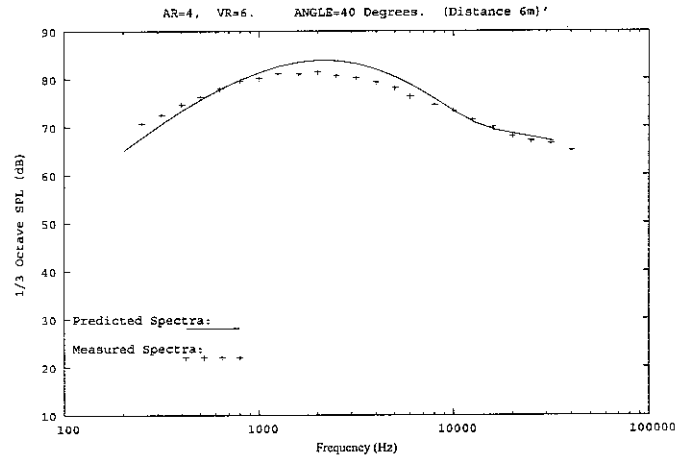

(b) Spectrum at 40° to jet axis.

Figure 4: Spectra for an Area Ratio 4, Velocity Ratio 0.6 Jet at various angles to the jet axis.

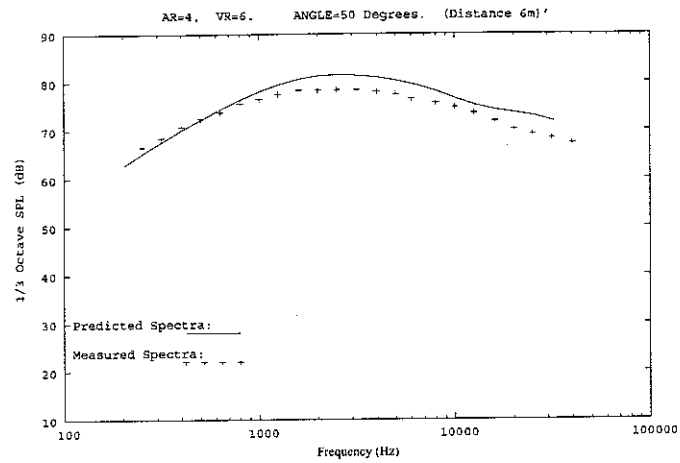

(c) Spectrum at 50° to jet axis.

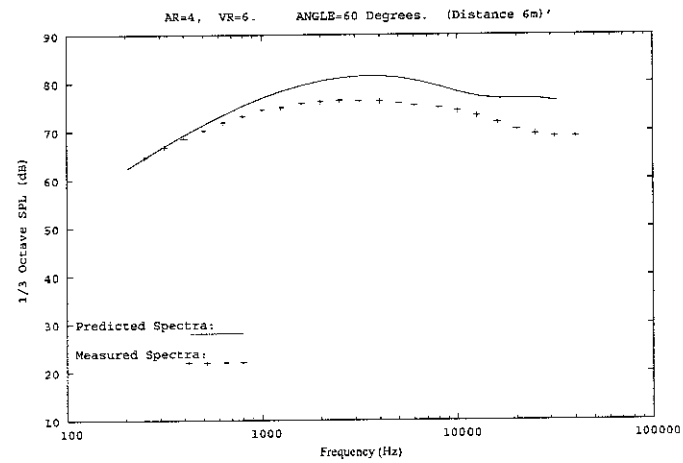

(d) Spectrum at 60° to jet axis.

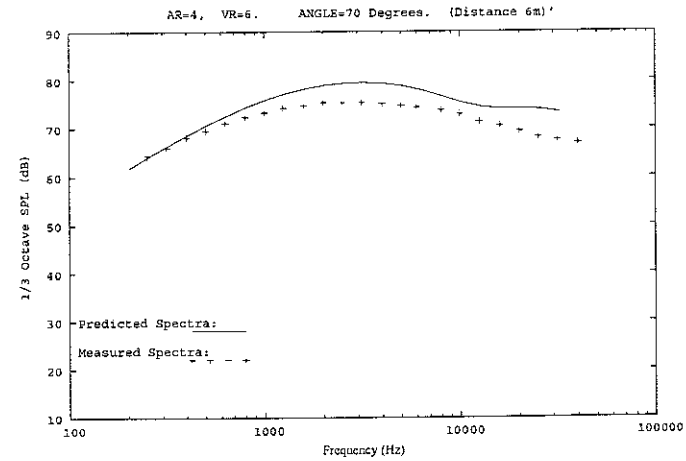

(e) Spectrum at 70° to jet axis.

Figure 4: (Contd.) Spectra for an Area Ratio 4, Velocity Ratio 0.6 Jet at various angles to the jet axis.

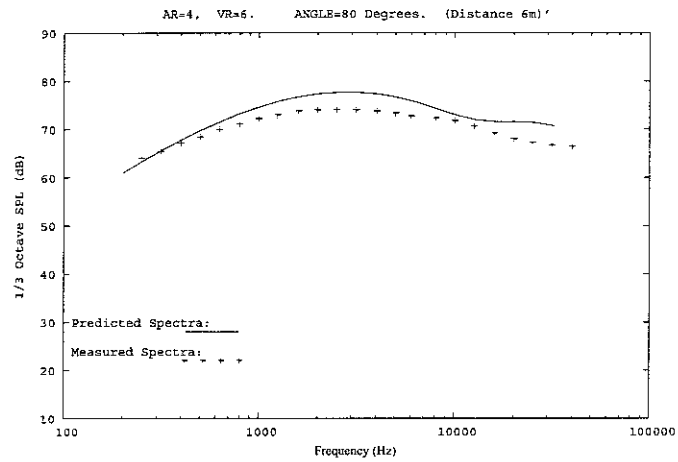

(f) Spectrum at 80° to jet axis.

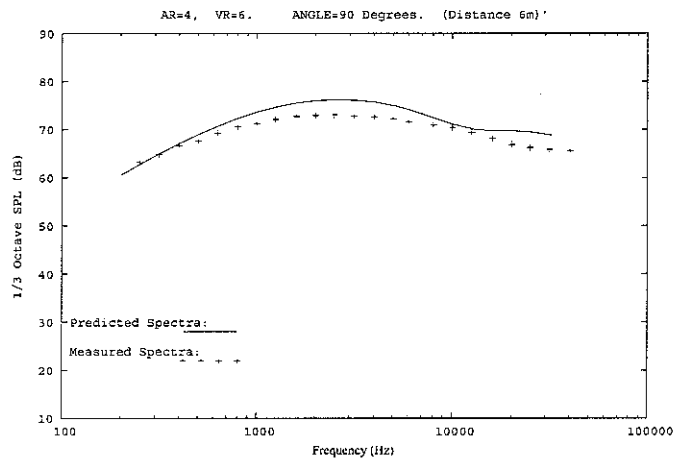

(g) Spectrum at 90° to jet axis.

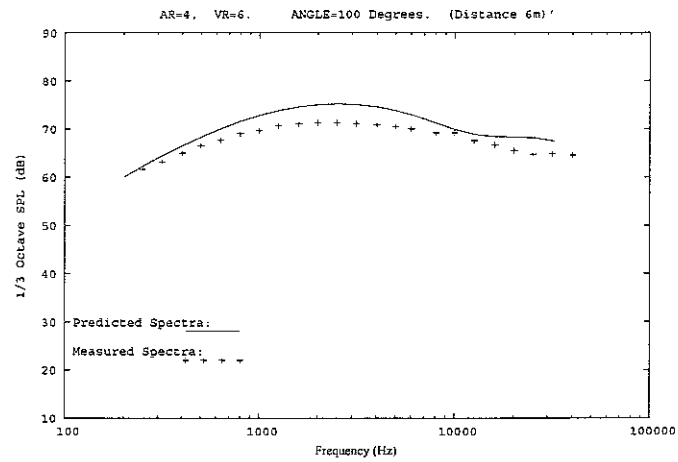

(h) Spectrum at 100° to jet axis.

Figure 4: (Contd.) Spectra for an Area Ratio 4, Velocity Ratio 0.6 Jet at various angles to the jet axis.

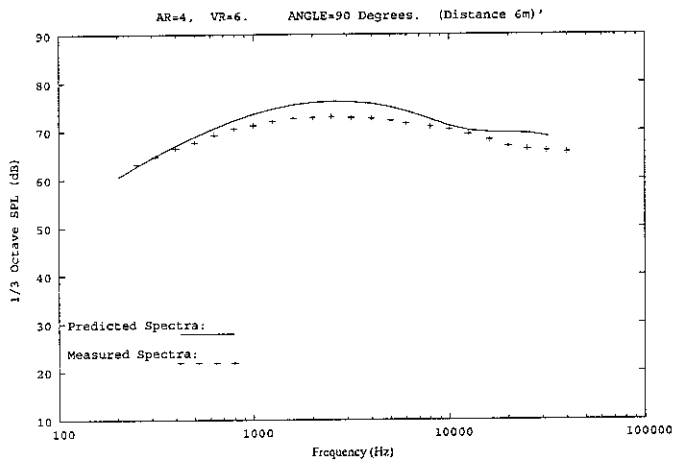

(i) Spectrum at 110° to jet axis.

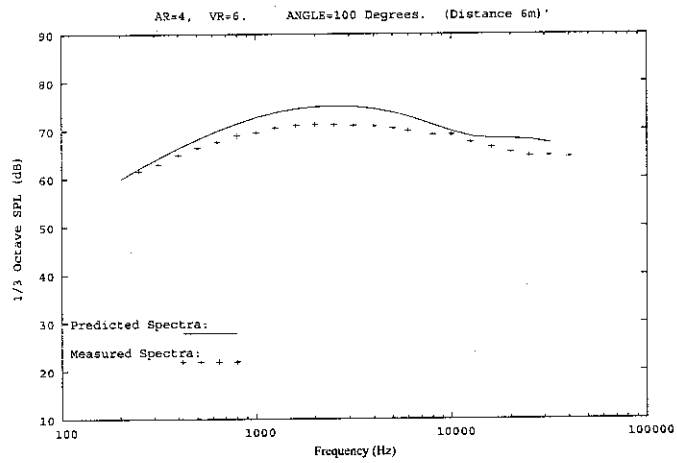

(j) Spectrum at 120° to jet axis.

Figure 4: (Contd.) Spectra for an Area Ratio 4, Velocity Ratio 0.6 Jet at various angles to the jet axis.

8.4 Area ratio 4, Velocity ratio 0.8 spectra comparisons

The comparisons for an area ratio 2 jet with a velocity ratio of 0.6 are shown in Figure 5 (a)–(j) below.

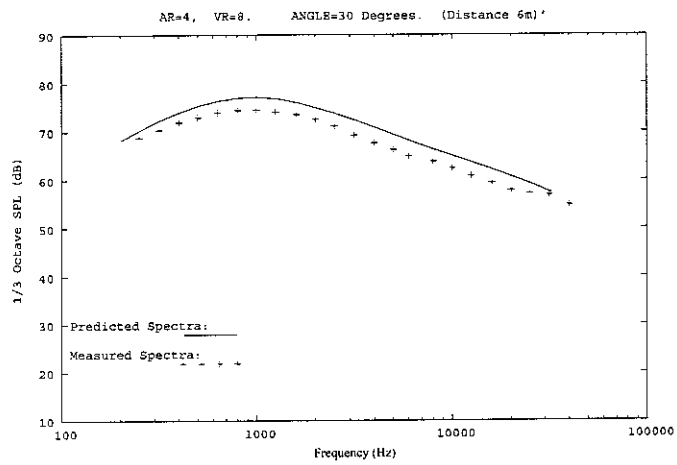

(a) Spectrum at 30° to jet axis.

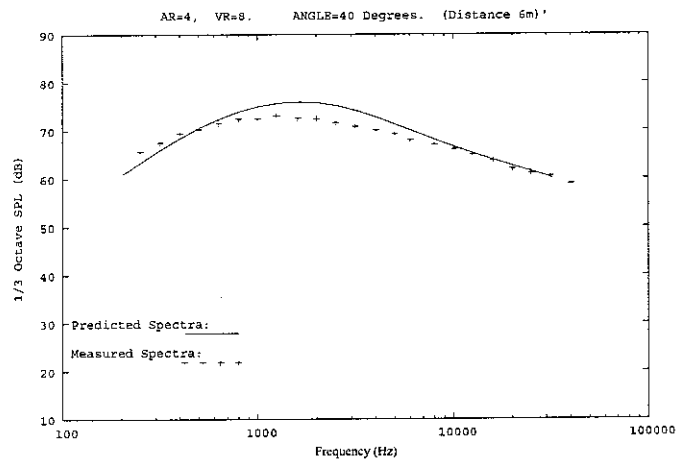

(b) Spectrum at 40° to jet axis.

Figure 5: Spectra for an Area Ratio 4, Velocity Ratio 0.8 Jet at various angles to the jet axis.

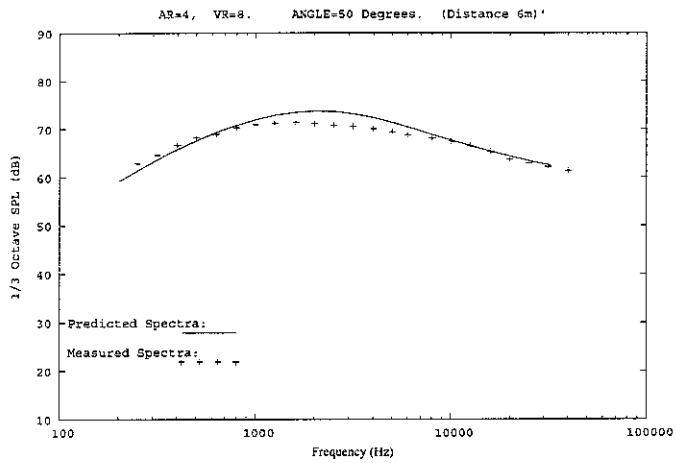

(c) Spectrum at 50° to jet axis.

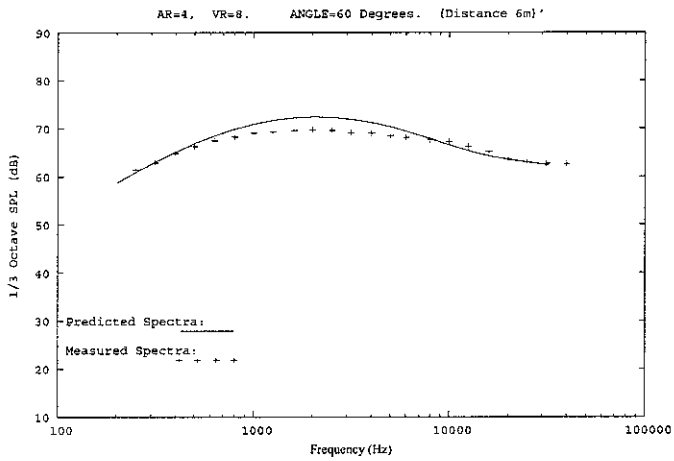

(d) Spectrum at 60° to jet axis.

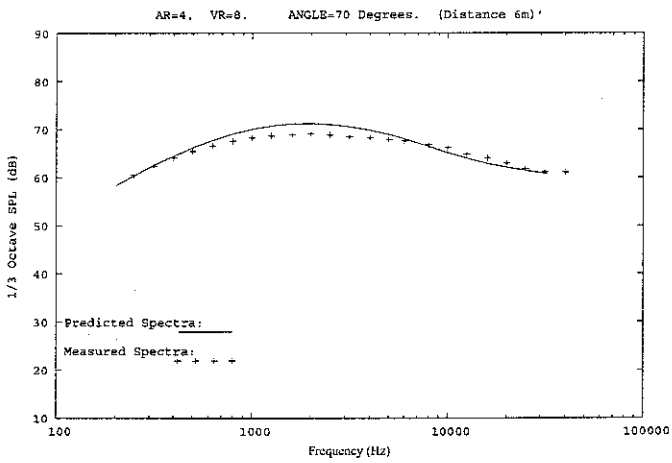

(e) Spectrum at 70° to jet axis.

Figure 5: (Contd.) Spectra for an Area Ratio 4, Velocity Ratio 0.8 Jet at various angles to the jet axis.

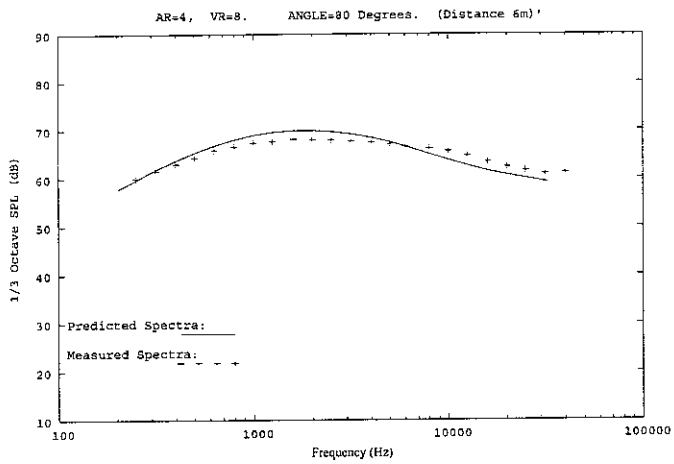

(f) Spectrum at 80° to jet axis.

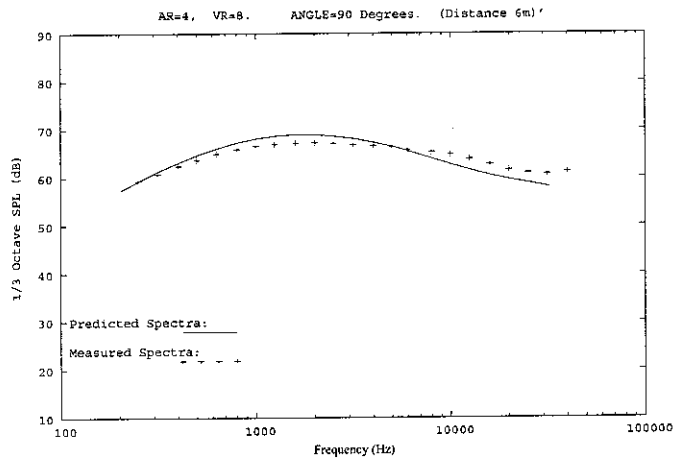

(g) Spectrum at 90° to jet axis.

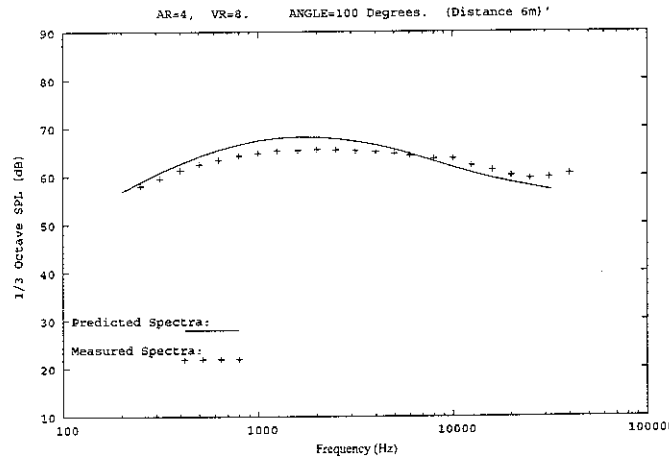

(h) Spectrum at 100° to jet axis.

Figure 5: (Contd.) Spectra for an Area Ratio 4, Velocity Ratio 0.8 Jet at various angles to the jet axis.

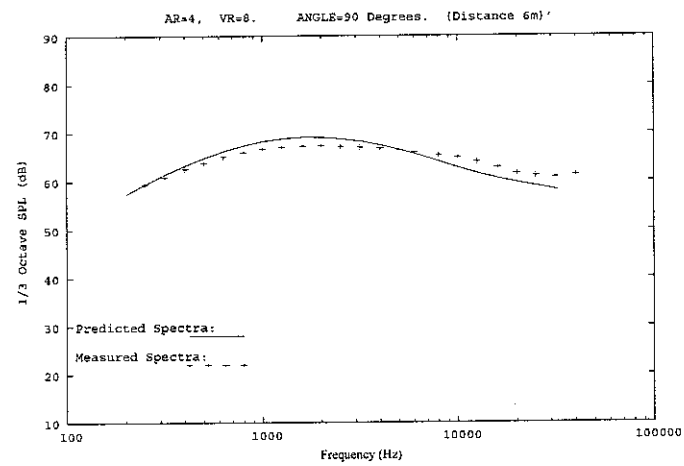

(i) Spectrum at 110° to jet axis.

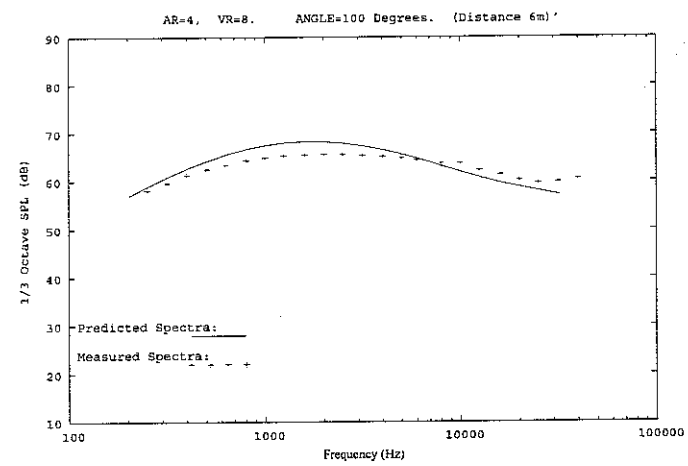

(j) Spectrum at 120° to jet axis.

Figure 5: (Contd.) Spectra for an Area Ratio 4, Velocity Ratio 0.8 Jet at various angles to the jet axis.

9 Comparison of predicted and measured source distributions

Equation (77) was used to compute the axial source strength density distribution at a number of the 1/3 octave centre frequencis. These were then normalised,

$$\overline{q}(x,f) = \frac{q(x,f)}{\int_0^\infty q(x,f)\,dx} \tag{79}$$

and compared with normalised source distributions obtained experimentally using a polar correlation [5] based technique as described in reference [2].

Polar Correlation uses cross-spectral measurements between a series of microphones laid out in a polar arc centred on the jet nozzle to form an image of the source strength distribution q along the jet axis. It is based on the fact that, for an axial distribution of incoherent sources there is an inverse Fourier relationship between the normalized cross-spectrum C at points on a polar arc and the source strength distribution q along the jet axis:

$$C(\alpha,\omega) = \int_{-\infty}^{\infty} q(x,\omega)\exp(-ikx\sin\alpha)\,dx \tag{80}$$

where α is the polar angle from the reference microphone at 90°. In principle this relationship can be inverted to give the source distribution image as an integral over $k\sin\alpha$, but in practice the restricted angular range over which measurements are taken leads to a resolution limited image of the true source distribution. Additionally, the finite number of microphones used in the array leads to aliasing problems that restricts the frequency range that can be analysed successfully. For the test conditions considered here source distributions were measured for frequencies in the range of $200Hz$–$20000Hz$. Full details of the experiments are given in reference[2].

For each of the four test conditions a comparison between predicted and measured source strength distributions at frequencies nominally equal to 1,2,4,8 and 16KHz is given.[3] In all the diagrams that follow, the predicted source density is shown in red and the measured source image in green. When viewing these figures it should be borne in mind that the measured distributions are always likely to be relatively broad because of the windowing algorithm used in the data analysis. Also, normalised source distributions are being plotted, and for the measured distributions, this normalisation will be relative to a *noise floor* that extends over the entire window (sometimes up to 200 diameters downstream from the nozzle). Thus, only the position of source maxima and the overall shapes of the curves can be usefully compared.

To differentiate different portions of the jet that correspond to the component jets as used in the Four Source Model discussed below, blue arrows indicate the (approximate) positions of the end of the secondary and primary potential cores as predicted by the CFD mean flow calculation.

[3]The exact frequencies used were $1015.9Hz$, $2031.9Hz$, $4063.7Hz$, $8127.5Hz$ and $16255.0Hz$.

9.1 Area Ratio 2, Velocity Ratio 0.6 source distribution comparisons

The comparisons for an area ratio 2 jet with a velocity ratio of 0.8 are shown in Figure 6 (a) – (e) below.

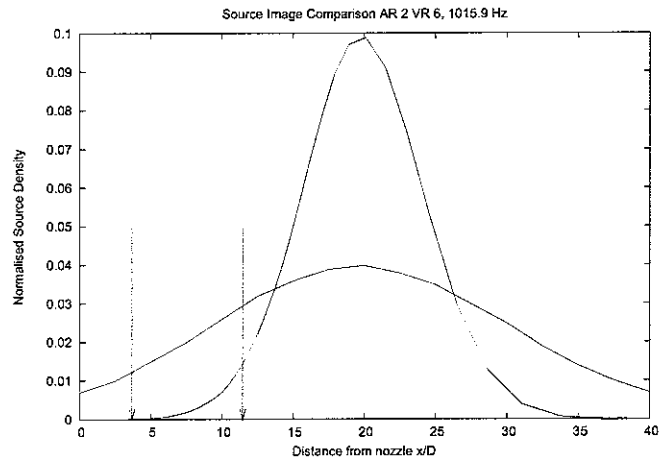

(a) Source distributions at $f = 1015.9Hz$

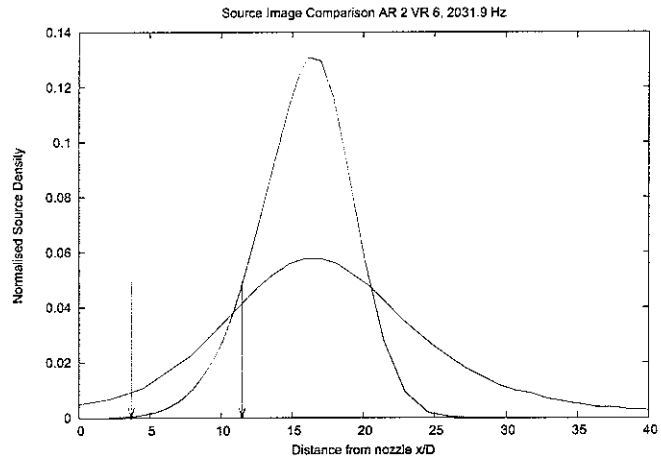

(b) Source distributions at $f = 2031.9Hz$

Figure 6: Predicted (red) *v.* measured (green) source distributions: $A_s/A_p = 2$, $V_s/V_p = 0.6$.

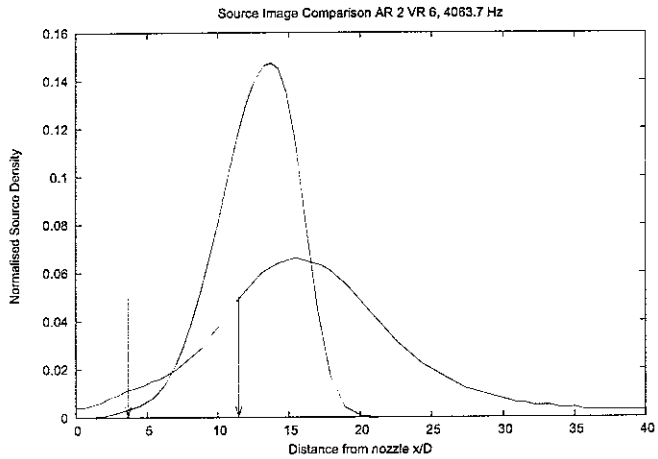

(c) Source distributions at $f = 4063.7Hz$

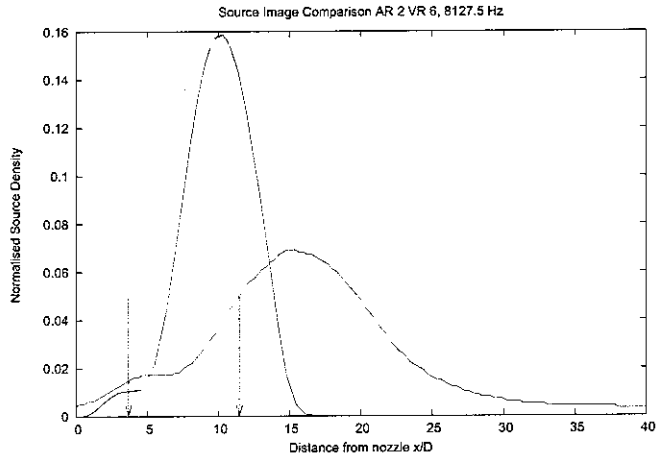

(d) Source distributions at $f = 8127.5Hz$

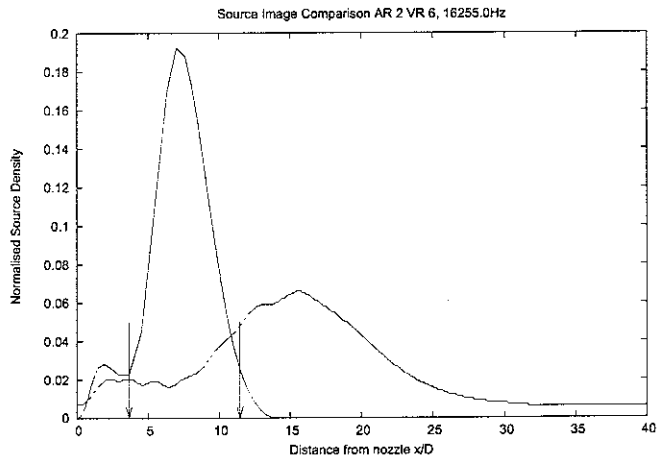

(e) Source distributions at $f = 16\ ,255.0Hz$

Figure 6: (Contd.) Predicted (red) *v.* measured (green) source distributions: $A_s/A_p = 2$, $V_s/V_p = 0.6$.

9.2 Area ratio 2, Velocity ratio 0.8 source distribution comparisons

The comparisons for an area ratio 2 jet with a velocity ratio of 0.8 are shown in Figure 7 (a) – (e) below.

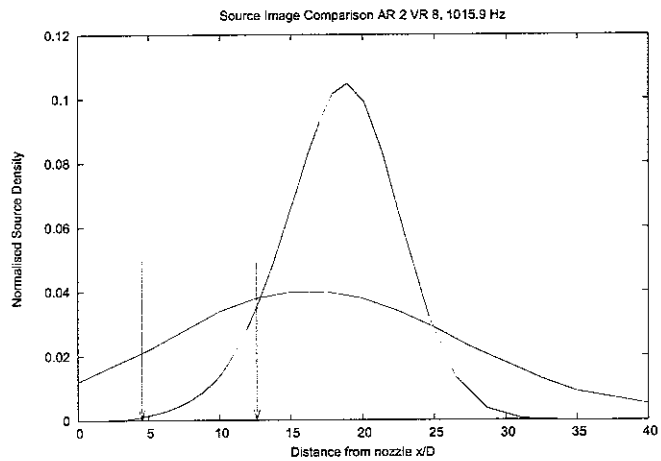

(a) Source distributions at $f = 1015.9Hz$

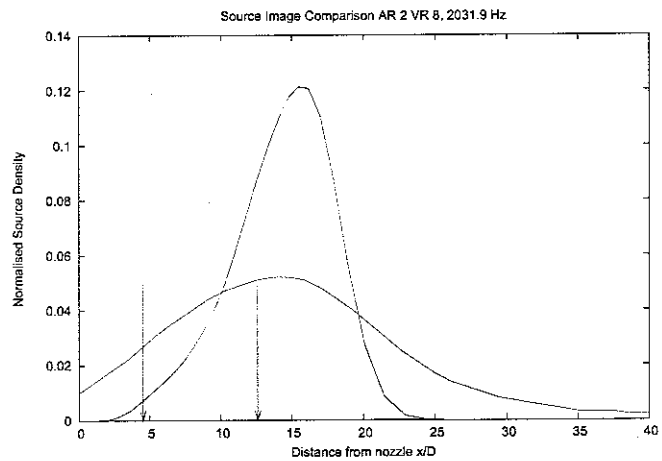

(b) Source distributions at $f = 2031.9Hz$

Figure 7: Predicted (red) *v.* measured (green) source distributions: $A_s/A_p = 2$, $V_s/V_p = 0.8$.

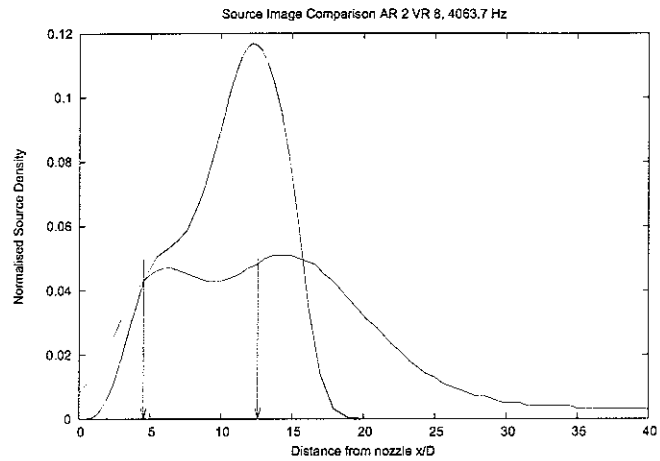

(c) Source distributions at $f = 4063.7Hz$

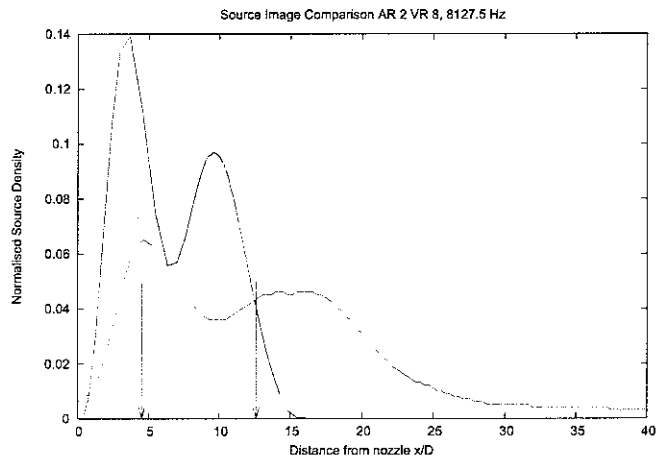

(d) Source distributions at $f = 8127.5Hz$

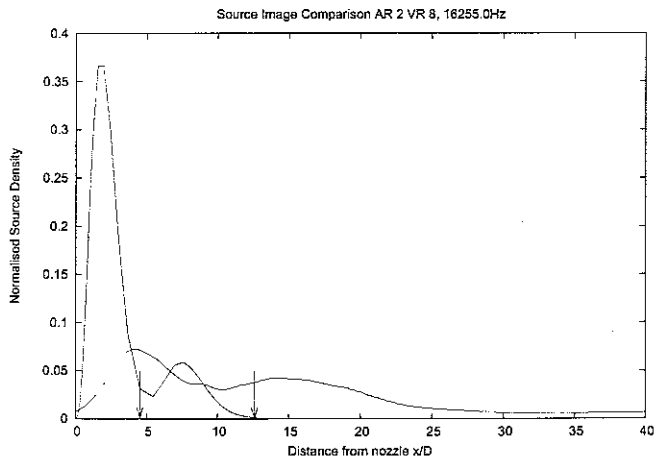

(e) Source distributions at $f = 16\ ,255.0Hz$

Figure 7: (Contd.) Predicted (red) *v.* measured (green) source distributions: $A_s/A_p = 2$, $V_s/V_p = 0.8$.

9.3 Area ratio 4, Velocity ratio 0.6 source distribution comparisons

The comparisons for an area ratio 2 jet with a velocity ratio of 0.8 are shown in Figure 8 (a) – (e) below.

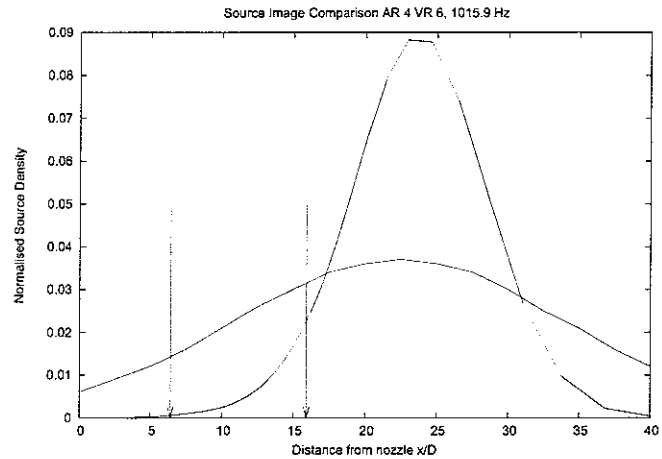

(a) Source distributions at $f = 1015.9Hz$

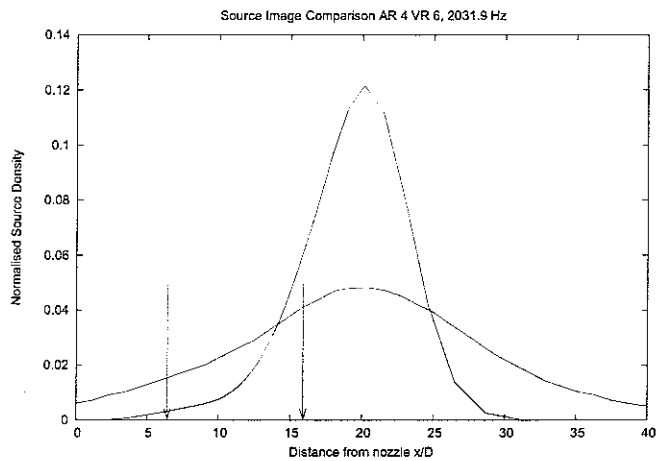

(b) Source distributions at $f = 2031.9Hz$

Figure 8: Predicted (red) *v.* measured (green) source distributions: $A_s/A_p = 4$, $V_s/V_p = 0.6$.

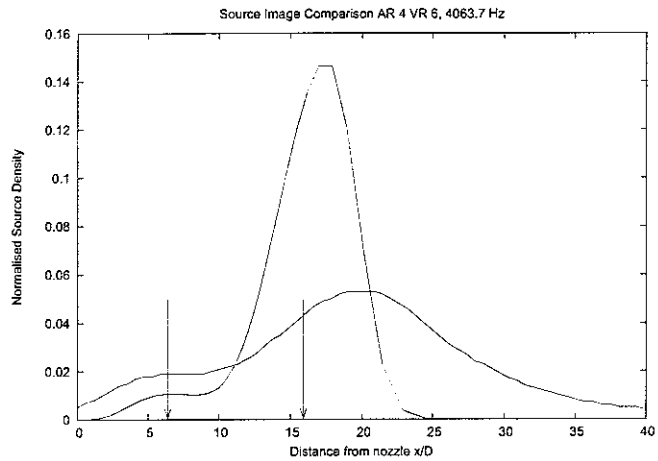

(c) Source distributions at $f = 4063.7Hz$

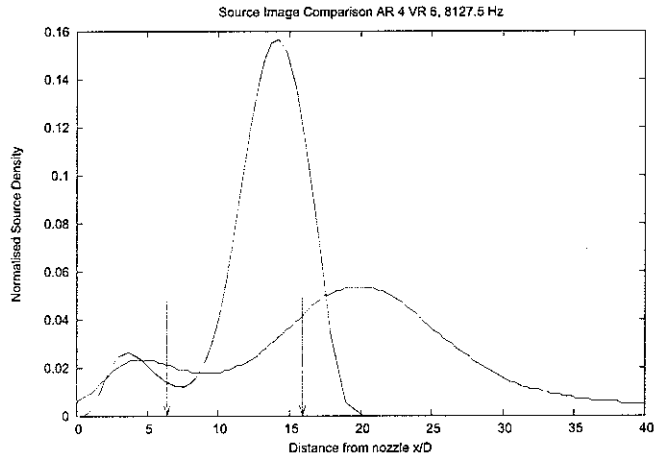

(d) Source distributions at $f = 8127.5Hz$

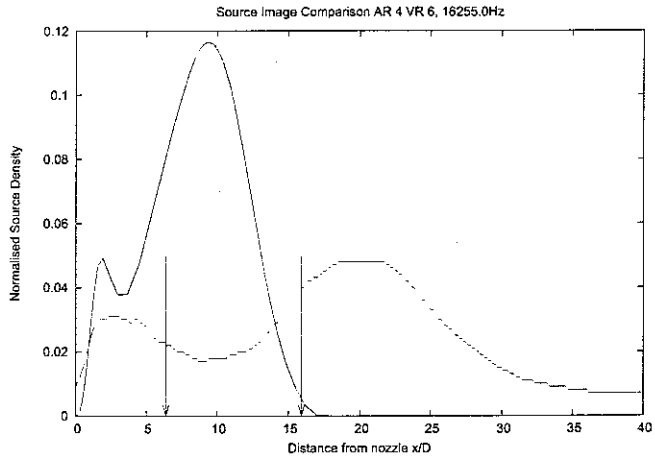

(e) Source distributions at $f = 16\ ,255.0Hz$

Figure 8: (Contd.) Predicted (red) *v.* measured (green) source distributions: $A_s/A_p = 4$, $V_s/V_p = 0.6$.

9.4 Area ratio 4, Velocity ratio 0.8 source distribution comparisons

The comparisons for an area ratio 2 jet with a velocity ratio of 0.8 are shown in Figure 9 (a) – (e) below.

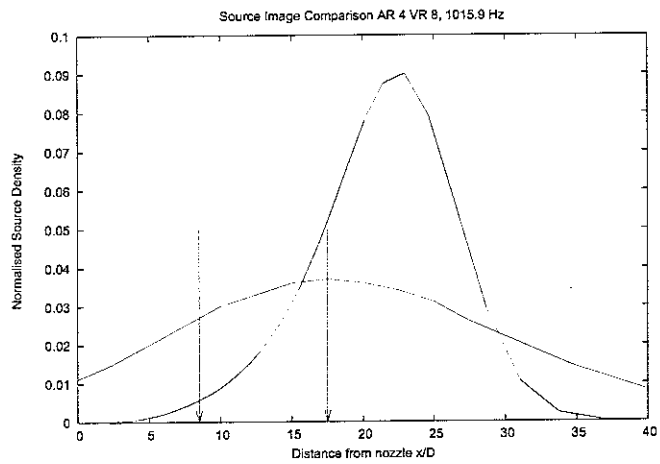

(a) Source distributions at $f = 1015.9Hz$

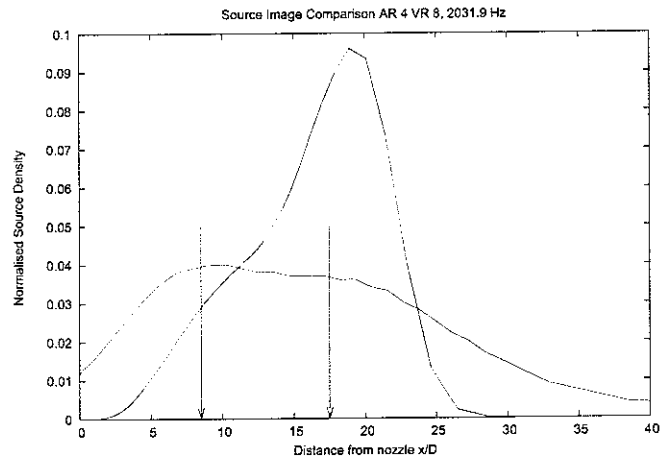

(b) Source distributions at $f = 2031.9Hz$

Figure 9: Predicted (red) *v.* measured (green) source distributions: $A_s/A_p = 4$, $V_s/V_p = 0.8$.

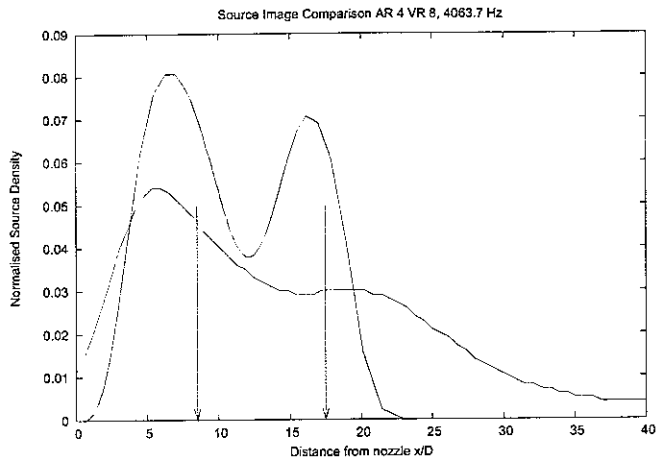

(c) Source distributions at $f = 4063.7Hz$

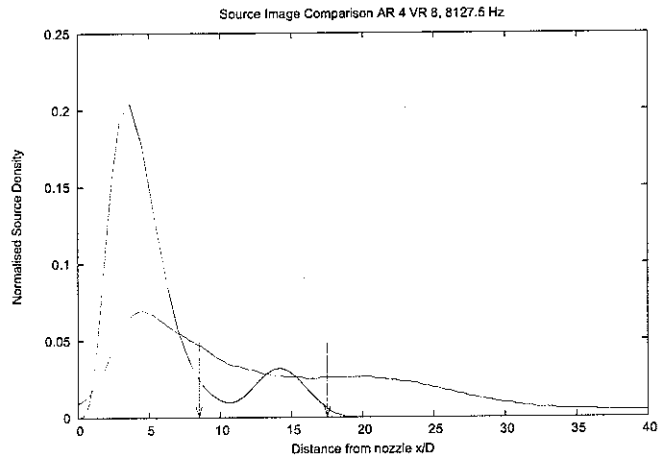

(d) Source distributions at $f = 8127.5Hz$

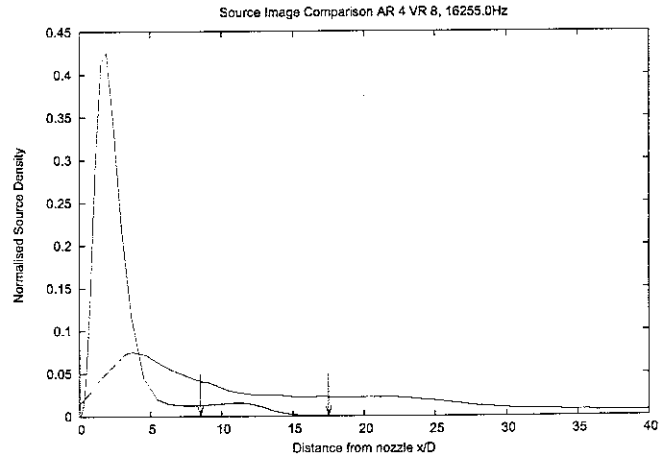

(e) Source distributions at $f = 16\ ,255.0Hz$

Figure 9: (Contd.) Predicted (red) *v.* measured (green) source distributions: $A_s/A_p = 4$, $V_s/V_p = 0.8$.

10 Comparison of predictions with CAJEN calculations

CAJEN is an empirically based coaxial jet noise prediction code that implements the Four Source Model [6, 7]. In turn the rational for the empirically based Four Source Model comes from measurements of the mean and turbulent velocities of coaxial jets made by Ko and Kwan [12]. They were able to identify regions of a coaxial jet flow where the flow variables scaled like those of an equivalent single jet. The Four Source Method utilises this observation by identifying such regions as acoustic sources that radiate sound in the same way as sections of the equivalent single stream jets. In this way the spectrum of the coaxial jet can be built up from appropriately filtered single stream jet spectra, which are in turn available from a relatively compact database of single stream jet spectra.

The component aerodynamic structure of a coaxial jet as envisaged by the Four Source Model is illustrated in Figure 10 below. Close to the nozzle there exists an initial mixing region that contains the potential cores of both the primary and secondary jets. This terminates at the downstream end of the potential core of the secondary annulus flow. In the far downstream region of the jet, beyond the end of the potential core of the primary jet, the flow will approach that which would pertain if the primary and secondary jets had been mixed at the nozzle exit plane. Between these extremities, where the primary and secondary shear layers interact, is a region of complex flow known as the interaction region.

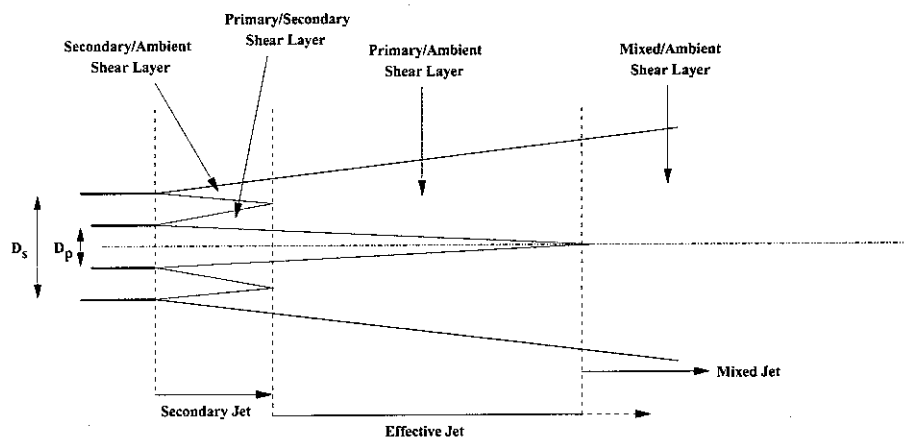

Figure 10: Schematic illustration of flow from a coplanar coaxial jet, showing the main mixing regions as defined in the Four Source Model.

The Four Source Model identifies each of these different regions with a portion of an equivalent single stream jet defined by the scaling velocity and nozzle diameter identified by Ko and Kwan. By assuming that the dominant frequency produced at any axial station of a single stream jet varies inversely to the distance from the nozzle, with a frequency corresponding to a Strouhal number of $St = 1$ being produced by the region at the end of the potential core it is possible to identify the spatial distribution of the component jets with a portion of their corresponding spectra. Making due allowance for the observed reduction in turbulence intensity in the interaction region, these partial spectra are summed to give a prediction for

the spectrum of the parent coaxial jet. Note that the source corresponding to the mixing region between the primary and secondary potential cores can be shown to be insignificant and is ignored. This leaves the main acoustic sources to be summed as the *secondary jet*, the *equivalent jet* and the *mixed jet* as shown in Figure 11.

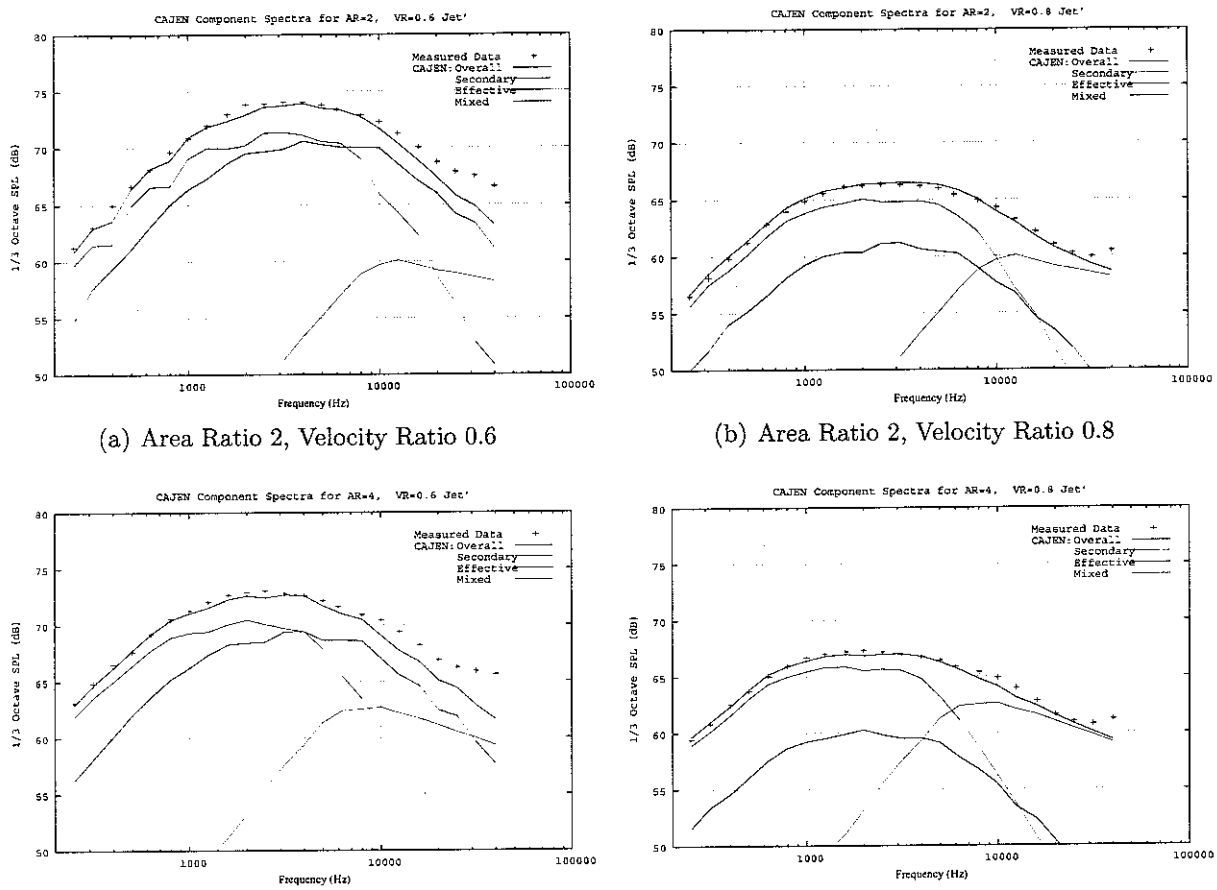

(a) Area Ratio 2, Velocity Ratio 0.6

(b) Area Ratio 2, Velocity Ratio 0.8

(c) Area Ratio 4, Velocity Ratio 0.6

(d) Area Ratio 4, Velocity Ratio 0.8

Figure 11: CAJEN Predicted Spectra for the four jet configurations considered

To obtain a normalised source strength from the CAJEN predicted Sound Pressure Levels we need only take antilogarithms and appropriately normalise to give three source strengths, $Q_{sec}(f)$, Q_{eff} and Q_{mix} (say) for each of the component jets as a function of frequency. Also, by splitting the integration region in equation (79), a normalised source strength can be computed for each of the regions that correspond to the CAJEN component jets. Thus:

$$\overline{q}_{sec}(f) = \frac{\int_0^{\mathrm{SPC}} q(x,f)}{\int_0^{\infty} q(x,f)\,dx}, \qquad \overline{q}_{eff}(f) = \frac{\int_{\mathrm{SPC}}^{\mathrm{PPC}} q(x,f)}{\int_0^{\infty} q(x,f)\,dx}, \qquad \overline{q}_{mix}(f) = \frac{\int_{\mathrm{PPC}}^{\infty} q(x,f)}{\int_0^{\infty} q(x,f)\,dx}, \tag{81}$$

give a measure of the calculated source strength within the region up to the end of the secondary potential core (SPC); between the secondary potential core and the primary potential core (PPC); and downstream of the primary potential core. These source strengths are compared for each of the four jets studied in Figure 12.

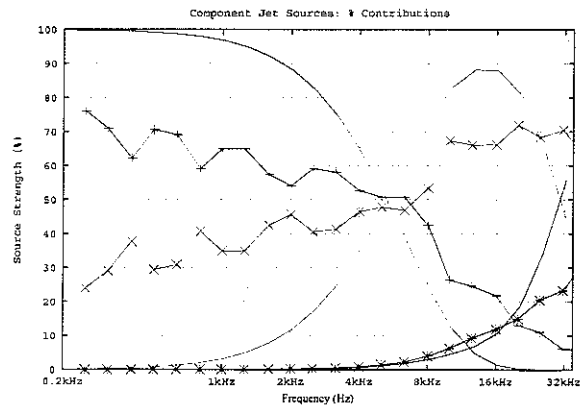

(a) Area Ratio 2; Velocity Ratio 0.6

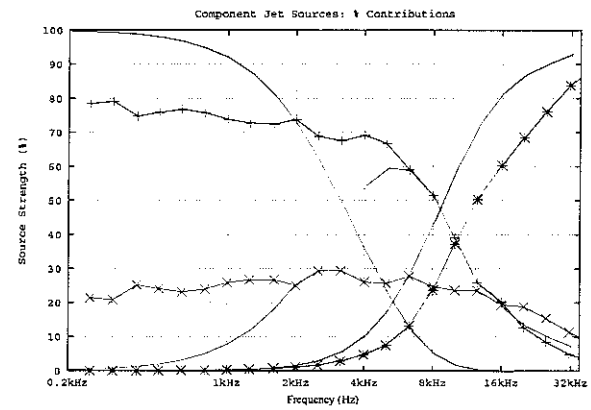

(b) Area Ratio 2; Velocity Ratio 0.8

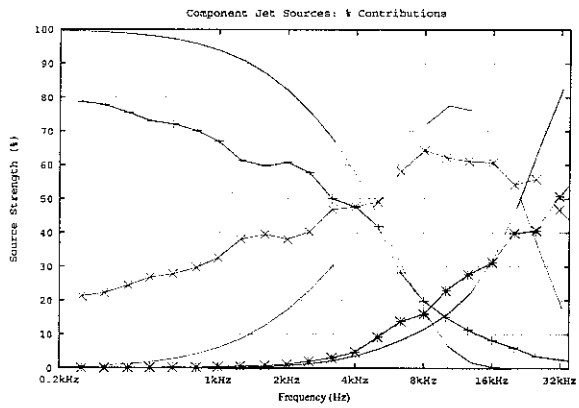

(c) Area Ratio 4; Velocity Ratio 0.6

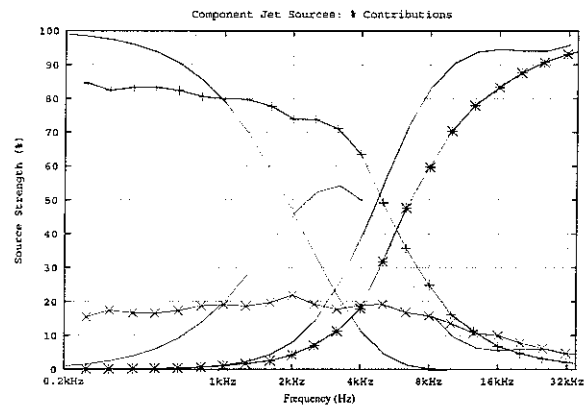

(d) Area Ratio 4; Velocity Ratio 0.8

Figure 12: Comparison of CAJEN component jet source densities and "equivalent" component jets for the present model (see text). Red lines are the mixed jet; green lines the effective jet; and blue lines the secondary jets. The lines come in pairs with CAJEN predictions discriminated by superposed symbols.

11 Discussion of Results

Spectra

Generally, the overall fit between prediction and measured spectra is good. The one exception is the Area Ratio 4, Velocity Ratio 0.6 jet, where the theory significantly over-predicts the intensity in the mid to high frequency range at angles above 50°. It is not clear why this should be the case, but notice that the same tendency is evident in the Area Ratio 2, Velocity Ratio 0.6 jet. In all cases the theory slightly over-predicts in the mid-frequency range (around $f \sim 3\text{k}Hz$).

The two Velocity Ratio 0.8 jets are better predicted than the Velocity Ratio 0.6 jets, with the Area Ratio 4, Velocity ratio 0.8 giving the best fit to the data. This may not be surprising because, intuitively, this jet configuration gives a flow that most closely resembles a single-stream jet flow.

In all the cases considered, the predicted spectra broadly show the same variation with angle as do the measured spectra. This is important because as we vary the observation angle from 30° forward we move from deep inside the cone of silence out up to 90° where directional effects no longer exist. Thus, not only does the theory correctly model the source strengths, it also captures the essential physics involved in determining the directivity of jets.

Source Distributions

Measured source images of coaxial jets generally show a single peak for low frequencies that develops into a double peaked curve as the frequency increases. This trend is also seen in the predicted source distributions. For low frequencies, both the position of the peak and the overall shape of the image is predicted well. (As stated above, the measured images will always appear broader than the actual sources.) As the frequency rises the general behaviour of the measured distributions is well reflected by the theoretical distributions, but the latter have a tendency to shift upstream towards the nozzle more quickly than the measured distributions do.

For example, in the Area Ratio 2, Velocity Ratio 0.6 case, the predicted and measured maximum source density correspond almost exactly at $1\text{k}Hz$, (Figure 6a), but at $4\text{k}Hz$ the theoretical prediction gives the source maximum at a point some 3 primary diameters closer to the nozzle than the measured source, (Figure 6c). Notice however, how well the shape of the curves correspond, with both theoretical prediction and measured image having the same slight asymmetry. This asymmetry marks the appearance of an upstream noise source that is important at higher frequencies and is clearly evident at $8\text{k}Hz$ and $16\text{k}Hz$, (Figures 6d & 6e). These trends are also seen in the other comparisons, Figures 7, 8 and 9.

Before concluding that the theoretical source distributions are positioned too far upstream, there are reasons to suggest that the assumptions inherent in obtaining the measured source images may tend to place the images too far downstream. Firstly, the polar correlation technique strictly applies only to a distribution of incoherent sources with identical directivity and this is clearly untrue in the present case. Secondly, sound being refracted by a shear layer will not only have it's angle of propagation altered, but will also emerge from the shear layer at a different axial position than it is produced (this being more pronounced at higher

frequencies). It is not possible to judge the likely significance of either of these effects without further study.

Comparison with CAJEN Calculation

The comparison between the inferred strengths of the CAJEN component jets and the predictions of the present model for the source strengths integrated over a corresponding region of flow gives good overall agreement for the Velocity Ratio 0.6 jets, (Figures 12a & 12c). At low frequencies both CAJEN and the theoretical curves show the mixed jet as dominating.[4] As the frequency rises the crossover between mixed jet dominating and effective jet dominating is correctly predicted, as is the rise in strength of the secondary jet. In both cases, the peak in effective jet strength is matched. If we accept the Four Source Methodology at face value, then this peak (occuring between 8 and 16kHz) will be due to turbulent flow at axial positions lying between the end of the secondary potential core and the end of the primary potential core. Figures 6 and 8 clearly show predicted peaks in this region for these frequencies but this is not reflected in the measured source distributions.

The Velocity Ratio 0.8 jets, Figures 12b & 12d, are somewhat problematic. While these jets may intuitively be considered to most resemble a single stream jet, CAJEN predicts that there is no frequency for which the effective jet region represents the dominant source. On the other hand, the present model predicts this region as being the peak source for frequencies in the mid range, as one might expect from a single-stream analogy. However, we note that the CAJEN source distributions would be expected to match the measured source distributions more closely than the present model distributions, with a peak source remaining downstream of the end of the primary potential core. We also note how well the high frequency tail of the predicted effective jet matches the fall-off of the CAJEN *mixed* jet.

[4]In the Four Source Method [6, 7] there is no low frequency cut-off for the effective jet that therefore contributes at all frequencies. Hence we should compare the predicted source at low frequencies with the *sum* of the effective and mixed jet sources as given by CAJEN.

12 Conclusions

A RANS CFD based model has been described and used to predict the far field noise spectra and noise source distributions for a number of isothermal coplanar coaxial jets configurations.

While the predicted spectra and source distributions clearly indicate that the theory has correctly captured the main physics of problem the systematic discrepancies point to the need for further work.

A number of fairly gross assumptions have been made within the present model and these should be investigated, notably the various approximations in the calculation of the flow factor need to be addressed by a more detailed theoretical analysis. This is especially true if the theory is to be extended to heated jet flows. (In deriving the high frequency Flow Factor an assumption was made that only one turning point exists. This is already a questionable assumption but is very unlikely to be true for flows where a temperature gradient is also present.)

Flow-directivity effects, however, are not apparent at 90° to the axis, and the problem of source distribution position is therefore not related any such approximations. One possible explanation may be that the wrong calibration constants have been chosen and this will be investigated by a systematic optimisation routine. Another possible (and more likely) explanation is the failure of the present model to differentiate between axial and transverse lengthscales. Turbulence in jet flows is known to be anisotropic so the assumption used in the model (equation 24) is unlikely to be correct. It is therefore proposed that more general models as represented by equation (25) be investigated. However, to clarify this issue completely requires more experimental data than is presently available.

13 Acknowledgements

The author wishes to thank Paul Strange of Rolls-Royce, and Craig Mead and Marcus Harper-Bourne of QinetiQ and for their help and useful discussions. Thanks are also due to Gary Page and Jim McGuirk of Loughborough University for providing the CFD data; to Alessandro Bassetti for the CAJEN data; and to Juan Battener-Moro for providing the measured source distributions.

References

[1] T.F. Balsa and P.R. Gliebe. Aerodynamics and noise of coaxial jets. *AIAA Journal*, 15:1550–1558, 1977.

[2] J.P. Battaner-Moro. New automated source breakdown algorithm for jet noise. AIAA Paper 2003–3324, May 2003. 9th AIAA/CEAS Aeroacoustics Conference and Exhibit, Hilton Head, South Carolina.

[3] C.M. Bender and S.S. Orzag. *Advanced Mathematical Methods for Scientists and Engineers* International Edition. McGraw-Hill Book Company, Sinapore, 1978.

[4] J.E. Ffowcs Williams. The noise from turbulence convected at high speed. *Proceedings of the Royal Society London, Series A*, 255:469–503, 1963.

[5] M.J. Fisher, M. Harper-Bourne, and S.A.L. Glegg. Jet engine noise source location: The polar correlation technique. *Journal of Sound and Vibration*, 51:23–54, 1977.

[6] M.J. Fisher, G.A. Preston, and W.D. Bryce. A modelling of the noise from simple coaxial jets, part 1: With unheated primary flow. *Journal of Sound and Vibration*, 209(3):385–403, 1998.

[7] M.J. Fisher, G.A. Preston, and C.J. Mead. A modelling of the noise from simple coaxial jets, part 2: With heated primary flow. *Journal of Sound and Vibration*, 209(3):405–417, 1998.

[8] M.E. Goldstein. *Aeroacoustics*. McGraw-Hill, New York, 1976.

[9] M. Harper-Bourne. Jet near field noise prediction. AIAA Paper 99–1838, May 1999. 5th AIAA/CEAS Aeroacoustics Conference, Seattle, WA.

[10] A. Khavaran. Computation of supersonic jet mixing noise for an axisymmetric convergent-divergent nozzle. *AIAA Journal of Aircraft*, 31:603–612, 1993.

[11] A. Khavaran. Role of anisotropy in turbulent mixing noise. *AIAA Journal*, 37:832–841, 1999.

[12] N.W.M. Ko and A.S.H. Kwan. The initial region of subsonic coaxial jets. *Journal of Fluid Mechanics*, 73:305–332, 1976.

[13] M.J. Lighthill. On sound generated aerodynamically: Part 1. General theory. *Proceedings of the Royal Society London, Series A*, 211:564–587, 1953.

[14] M.J. Lighthill. On sound generated aerodynamically: Part 2. Turbulence as a source of sound. *Proceedings of the Royal Society London, Series A*, 214:1–32, 1954.

[15] G.M. Lilley. The generation and radiation of supersonic jet noise. vol. iv – theory of turbulence generated noise, noise radiation from upstream sources, and combustion noise. United States Air Force Aero Propulsion Laboratory Technical Report TR–72–53, 1972.

[16] P.A. Lush. Measurements of subsonic jet noise and comparisons with theory. *Journal of Fluid Mechanics*, 46:477–500, 1971.

[17] M.J.Fisher and P.O.A.L. Davies. Correation measurements in a non-frozen pattern of turbulence. *JFM*, 18:97–116, 1963.

[18] P.J. Morris and F. Farassat. Acoustic analogy and alternative theories for jet noise prediction. *AIAA Journal*, 40:671–680, 2002.

[19] P.M. Morse and H. Feshbach. *Methods of Theoretical Physics*. McGraw-Hill, New York, 1953.

[20] Gary J. Page, James J. McGuirk, Mamdud Hossain, Nicola J. Hughes, and Miles T. Trumper. A computational and experimental investigation of serrated coaxial nozzles. AIAA Paper 2002–2554, June 2002. 8th AIAA/CEAS Aeroacoustics Conference, Breckingridge, Colorado.

[21] G.J. Page, J.J. McGuirk, M. Hossain, R.H. Self, and A. Bassetti. A CFD coupled acoustics approach for coaxial jet noise. AIAA Paper 2003–3286, May 2003. 9th AIAA/CEAS Aeroacoustics Conference and Exhibit, Hilton Head, South Carolina.

[22] T.F. Balsa R. Mani and P.R. Gliebe. High-velocity jet noise source location and reduction task 2. Federal Aviation Administration Report FAA-RD-76-II, 1978.

[23] H.S. Ribner. The generation of sound by turbulent jets. *Advances in Applied Mathematics*, 8:469–503, 1964.

[24] R.H. Self. Jet noise prediction using the Lighthill Acoustic Analogy. *Journal of Sound and Vibration*, 275:757–768, 2004.

[25] R.H. Self and A. Bassetti. A RANS based jet noise prediction scheme. AIAA Paper 2003–3325, May 2003. 9th AIAA/CEAS Aeroacoustics Conference and Exhibit, Hilton Head, South Carolina.

[26] C. K. W. Tam, N. Pastouchenko, and L. Auriault. Effects of forward flight on jet mixing noise from fine-scale turbulence. *AIAA Journal*, 39(7):1261–1269, July 2001.

[27] C.K.W. Tam and L. Auriault. Jet mixing noise from fine scale turbulence. *AIAA Journal*, 37(2):145–153, 1999.

[28] B.J. Tester and C.L. Morfey. Developments in jet noise modelling — theoretical predictions and comparisons with measured data. *Journal of Sound and Vibration*, 46(1):79–103, 1976.

[29] S.L. Woodruff, J.M. Seiner, M.Y. Hussaini, and G. Erlebacher. Implementation of new turbulence spectra in the Lighthill analogy source terms. *Journal of Sound and Vibration*, 242:197–214, 2001.